Magmatic evolution of the La Huerta Plutonic Complex, Jalisco: A 80–70 Ma record of arc magmatism along the Mexican Cordillera

Guillermo A. Ortiz-Joya[1,2], Peter Schaaf[1,*], Pedro Corona-Chávez[3], Gabriela N. Solís-Pichardo[4], Gerardo F. Arrieta-García[1], J. Teodoro Hernández-Treviño[1]

[1] Laboratorio Universitario de Geoquímica Isotópica (LUGIS), Instituto de Geofísica, Universidad Nacional Autónoma de México, Mexico City, Mexico.
[2] Posgrado en Ciencias de la Tierra, Universidad Nacional Autónoma de México, Mexico City, Mexico.
[3] Instituto de Investigaciones en Ciencias de la Tierra, Universidad Michoacana de San Nicolás de Hidalgo, Morelia, Mexico;
[4] LUGIS, Instituto de Geología, Universidad Nacional Autónoma de México, Mexico City, Mexico.
** pschaaf@geofisica.unam.mx*

ABSTRACT

The La Huerta Plutonic Complex (LHPC) forms part of the Cretaceous Mexican Cordillera, located between the well-documented ~80 Ma Puerto Vallarta Batholith (PVB) and the ~65 Ma Manzanillo Plutonic Complex (MPC). The LHPC shares lithological and geochemical features with the aforementioned batholiths and is dominated by voluminous granitoids and hybrid intrusions ranging from gabbro to granitic compositions. Scarce cummulitic gabbroic plutons are also present. Detailed petrographic, geochemical, microchemical, and geochronological results provide evidence for three magmatic stages: (1) a gabbroic magmatism at >84 Ma (observed from field relations), (2) ~83–80 Ma granitic magmatism (U-Pb in zircon), and (3) a ~75–70 Ma gabbroic and granitic magmatism (U-Pb in zircon). Thermobarometric determinations (3.0–2.0 kbar and <900 °C) and Sr-Nd isotopic signatures in all lithologies (εNd_i from +4.2 to +6.2 and $^{87}Sr/^{86}Sr_i$ around 0.7035) suggest a shallow magmatic environment with low and heterogeneous crustal assimilation. These features hold considerable differences with the northern PVB and are more comparable to the MPC. The LHPC is interpreted as the south easternmost part of the PVB and as a transitional zone between the PVB and the MPC.

Key words: Mexico; Cordillera; gabbros; geochronology; thermobarometry; paleotectonic evolution.

RESUMEN

Dentro de la Cordillera Cretácica Mexicana, el Complejo Plutónico La Huerta (LHPC) se encuentra entre el Batolito de Puerto Vallarta (PVB) y el Complejo Plutónico de Manzanillo (MPC), de ~80 Ma y ~65 Ma, respectivamente, con los cuales comparte algunas características geoquímicas e isotópicas. El LHPC está principalmente conformado por voluminosas intrusiones, compuestas de material gabroico a granítico con diferentes grados de hibridación, así como escasos gabros cumulíticos. Los resultados petrográficos, geoquímicos, microquímicos y geocronológicos muestran evidencia de al menos tres etapas magmáticas: (1) un evento gabroico en >84 Ma (relaciones de campo), (2) ~83–80 Ma magmatismo granítico (U-Pb en circón), y (3) un evento magmático gabroico a granítico de ~75–70 Ma (U-Pb en circón). Las estimaciones termobarométricas (3.0–2.0 kbar y <900 °C) junto con las firmas isotópicas Sr-Nd (εNd_i entre +4.2 y +6.2 y $^{87}Sr/^{86}Sr_i$ ~0.7035) muestran diferencias considerables con la porción norte del PVB mientras que se correlacionan mejor con el MPC, sugiriendo un nivel de emplazamiento somero con un bajo grado de asimilación cortical. Con base en los datos obtenidos, se interpreta al LHPC como parte de la porción oriental del PVB, en coexistencia y transición espacio-temporal con firmas geoquímicas correlacionables con el MPC, conformando una zona donde se puede observar la transición entre ambos cinturones magmáticos.

Palabras clave: México; Cordillera; gabros; geocronología; termobarometría; paleotectónica.

INTRODUCTION

Plutonic rocks are widely exposed along the Mexican Pacific coast. In general, these are I-type granitoids with granitic–granodioritic–tonalitic compositions ranging from Late Cretaceous to Paleogene (*e.g.*, Ortega-Gutiérrez *et al.*, 2014) related to the subduction of the Pacific Farallon and Cocos plates. During the last 20 years, increased accessibility and a large amount of new geochemical and geochronological data as well as new geological maps substantially improved the knowledge of Cordilleran plutonic rocks of the Guerrero tectonostratigraphic terrane (Campa and Coney, 1983; Centeno García *et al.*, 2008). An example is the Puerto Vallarta Batholith (PVB), formerly considered one of the largest Cretaceous granitic intrusions along the Mexican Pacific coast. However, recent findings in the northwestern area of the PVB demonstrate the presence of Jurassic and Cretaceous intrusions emplaced in metasedimentary and metaigneous sequences with maximum depositional ages ranging from 210 to 270 Ma and protolith precursor ages between 128 and 136 Ma, respectively (Valencia *et al.*, 2013; Schaaf *et al.*, 2020).

The PVB is subdivided into four blocks of which the La Huerta Plutonic Complex (LHPC) is the southernmost one (Figure 1a). Whereas

Ortiz-Joya, G.A. , Schaaf, P., Corona-Chávez, P., Solís-Pichardo, G.N., Arrieta-García, G.F., Hernández-Treviño, J.T., 2023, Magmatic evolution of the La Huerta Plutonic Complex, Jalisco: A 80–70 Ma record of arc magmatism along the Mexican Cordillera: Revista Mexicana de Ciencias Geológicas, v. 40, núm. 3, p. 273-293, DOI: 10.22201/cgeo.20072902e.2023.3.1766.

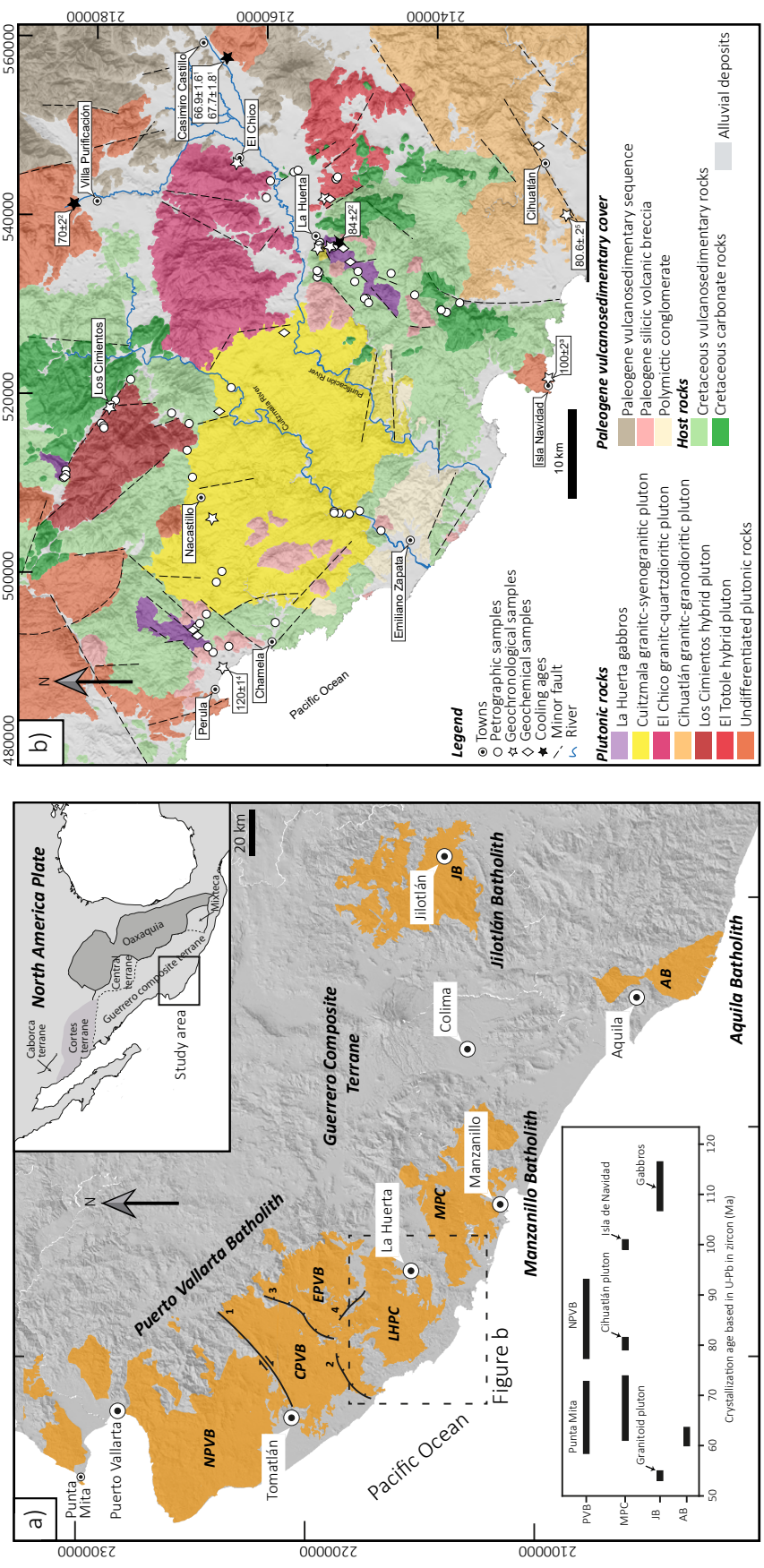

Figure 1. a) Map of south-western Mexico. The Guerrero Composite Terrane (Centeno-García *et al.*, 2008, 2011) hosts Cretaceous plutonic and volcanic arc-related rocks, exposed in four batholiths: Puerto Vallarta Batholith, Manzanillo Plutonic Complex, Jilotlán Batholith, and Aquila Batholith. The Puerto Vallarta Batholith (PVB) is divided into four areas: Northern Puerto Vallarta Batholith (NPVB), Central Puerto Vallarta Batholith (CPVB), Eastern Puerto Vallarta Batholith (EPVB), and La Huerta Plutonic Complex (LHPC). The tectonic limits are: 1. La Cumbre fault, 2. La Mesa fault, 3. California fault, 4. Tabaquero fault. The temporal framework of magmatic events in the four batholiths is shown in the inset, based on U-Pb zircon geochronology [after Panseri, 2007 (Isla Navidad, Manzanillo); Valencia *et al.*, 2013 (PVB); Villanueva-Lascurain *et al.*, 2016 (Jilotlán, JB); Salazar-Juárez, 2017 (Jilotlán, JB); Gómez Rivera, 2019 (Aquila, AB); Schaaf *et al.*, 2020 (PVB); Gutiérrez-Aguilar *et al.*, 2021a, 2021b (PVB); Schaaf *et al.*, 2022 (MPC)]. b) Geological map of the La Huerta Plutonic Complex. The locations and isotopic ages (in Ma) obtained from previous work are shown with superscript references: (1) Gastil *et al.*, 1976, (2) Solé *et al.*, 2007, (3) Panseri (2007), (4) Montaño Cortes *et al.* (2019) and (5) Schaaf *et al.* (2022).

a broad geological database is available for northern PVB rocks, such information is fragmentary for the south-central PVB. There is evidence for the emplacement of Late Cretaceous PVB granitoids and Early Cretaceous (~120 Ma) volcanic rocks of the Tecatitlán Formation in the Chamela-Perula area (Figure 1b; Montaño-Cortes *et al*., 2019). However, due to data scarcity, the southern PVB limits are poorly constrained. According to previous geological mapping and geochronological data (Panseri, 2007; Solé *et al*., 2007), the LHPC is composed of granitic rocks similar to the rest of the PVB blocks. On the other hand, gabbroic rocks close to the city of La Huerta were reported earlier (Schaaf, 1990), but their relationships are so far unknown.

In general, mafic plutonic rocks such as gabbros are scarce along the Mexican Cordilleran margin. Two occurrences are the ~115 Ma Jilotlan gabbro (Figure 1a; Villanueva-Lascurain *et al.,* 2016) and the ~65 Ma Manzanillo Plutonic Complex (Figure 1a; Schaaf *et al*., 2022). This is in contrast to the continuous gabbroic belt proposed by Gastil *et al*. (1976) along the NW Mexican Cordillera.

It is speculated that La Huerta gabbroic rocks share a common origin with the Manzanillo Plutonic Complex (MPC; Schaaf *et al*., 2022). Despite the similarities, no petrological studies from La Huerta gabbros and other plutonic rocks of the LHPC were performed. Therefore, the relationship of the LHPC to other PVB granitoids and gabbroic units such as those of the Jilotlán Batholith (Villanueva-Lascurain *et al*., 2016; Salazar-Juárez, 2017) and the Aquila Batholith (Gómez-Rivera, 2019; Figure 1a) remains unclear.

This work presents a geological map of the La Huerta Plutonic Complex (LHPC) between Perula and Cihuatlán (Figure 1b) accompanied by geochemical, geochronological, and thermobarometric data. Mineral abbreviations are based on Whitney and Evans (2010). We focus on gabbroic rocks in the La Huerta region and the relationship between the LHPC, Puerto Vallarta Batholith, and Manzanillo Plutonic Complex in order to comprehend the evolution of Cretaceous-Paleogene magmatism in this part of the Mexican Cordillera.

GEOLOGICAL AND TECTONIC SETTING OF THE LA HUERTA PLUTONIC COMPLEX

The LHPC covers an area of *ca*. 3600 km^2, located between the southern margin of the PVB and the MPC in the Zihuatanejo subterrane of the Guerrero terrane (Inset of Figure 1a; *e.g.*, Centeno-García *et al*., 2008, 2011). Based on a structural approach, the PVB can be divided into four regions separated by faults (Figure 1a). The northern PVB (NPVB) extends from Punta Mita and Puerto Vallarta to Tomatlán and is separated by the La Cumbre right-lateral fault from the Central PVB (CPVB). To t he southeast, the CPVB is separated from the La Huerta Plutonic Complex (LHPC) and the eastern PVB (EPVB) by NE-SW striking La Mesa and California normal faults, respectively. Finally, the LHPC and the EPVB are separated by the NW-SE tending Tabaquero fault. On the other hand, the southeastern limit with the MPC is not well exposed but an intrusive contact is suggested with the 80 Ma Cihuatlán granite and the gabbroic rocks of the MPC (Schaaf *et al*., 2022).

The host rock in the area is a Cretaceous volcano-sedimentary sequence composed of andesitic-rhyolitic tuffs and limestone intercalations. At the contact, it is common to observe a metamorphic aureole of marbles, cordierite-bearing quartz-feldspathic banded gneisses, and garnet- and epidote-bearing calcsilicates. Three groups of plutonic rocks constitute the LHPC and were mapped in detail (Figure 1b).

(1) The La Huerta gabbros conform the lower unit in the area and commonly occur in NE-SW oriented tabular bodies. Three gabbroic bodies were mapped (Figure 1b) composed of leucogabbros *sensu stricto* (*s.s.*) (Figure 2a, 2d), dikes of leucotroctolite, and norite (Figure 2b). The leucotroctolites are usually intercalated with basaltic dikes (Figure 2b). The boundaries with the host rock are irregular chilled margins with semi-vertical contacts that often constitute normal faults (Figure 1b).

(2) Three sub-circular-shaped and zoned granitoids were mapped: Cihuatlán, El Chico, and Cuitzmala (Figure 1b). The Cuitzmala pluton contains a core made of a biotite-monzogranite bordered by a syenogranitic variety. These rocks commonly exhibit quartz-dioritic to gabbroic mafic microgranular enclaves (MMEs) with ovoid and irregular shapes increasing their presence at the border of the pluton (Figure 2c). The El Chico pluton consists of a biotite-monzogranite that develops into a clinopyroxene (Cpx)- and orthopyroxene (Opx)-quartz-diorite at the border. Compared with the Cuitzmala pluton, this intrusive is poor in MMEs, which were only observed in the border with ovoid-shaped morphologies. The Cihuatlán pluton was previously studied by Schaaf (1990), Panseri (2007), and Schaaf *et al*. (2022) in a small region close to the city of Cihuatlán (Figure 1b), where it is mostly granodioritic in composition and contains scarce quartz-dioritic to hornblende-rich gabbroic MMEs. This intrusive was interpreted as part of the PVB due to geochemical and isotopic accordance and dated at ~80 Ma (zircon U-Pb age; Schaaf *et al*., 2022). The southeastern area of the Cihuatlán pluton is intruded by gabbroic to granodioritic pulses of the MPC (Schaaf *et al*., 2022).

The contact between the Cuitzmala granitic pluton and the La Huerta gabbros is characterized by chilled margins of quartz-diorite intruding the leucogabbros (Figure 2d), resulting in hybrid rocks with irregular portions of both lithologies and miarolitic cavities of K feldspar, pyroxene, and epidote, which evidence the consolidation of both plutonic bodies under *subsolidus* conditions (Figure 2e).

(3) Another group of hybridized intrusives shows mingling structures between gabbroic and granitic magmas, such as the Los Cimientos and El Totole plutons (Figure 1b; 2f–2h). The first one is a NW-SE-oriented tabular body mostly composed of hybrid quartz-diorites as a result of mingling between gabbros and granodiorites. Minor NW and SE portions are formed by coarse-grained biotite-granodiorites and quartz-diorites to granodiorites, respectively. Additionally, the SE portion hosts agglutinated ovoid-shaped gabbroic to dioritic enclaves of 10–20 cm length (Figure 2f).

The El Totole pluton is integrated by two lithologies, (1) an NW-SE oriented elongated coarse-grained hornblende-gabbro and (2) gabbro partially hybridized by the intrusion of an irregular-shaped monzogranite. The contact towards the granitic rocks is characterized by a chilled margin of fine-grained porphyritic gabbro, partly intruded by monzogranitic dikes, causing mafic dismemberment supported by the granites (Figure 2g). The porphyritic texture of the gabbros is related to the presence of K feldspar, probably transferred from the monzogranitic units (Figure 2h).

Other plutonic bodies, such as those close to Perula and Villa Purificación in the northern study area are not addressed in detail in this work, but their distribution and contact relationships are shown in the geological map (Figure 1b).

RESULTS

Petrography and mineral chemistry

Gabbroic rocks

The La Huerta gabbros are mostly composed of coarse-grained leucogabbros with 60–70 % tabular, cummulitic, euhedral Ca-rich plagioclase. The intercumulus phases are subhedral plagioclase,

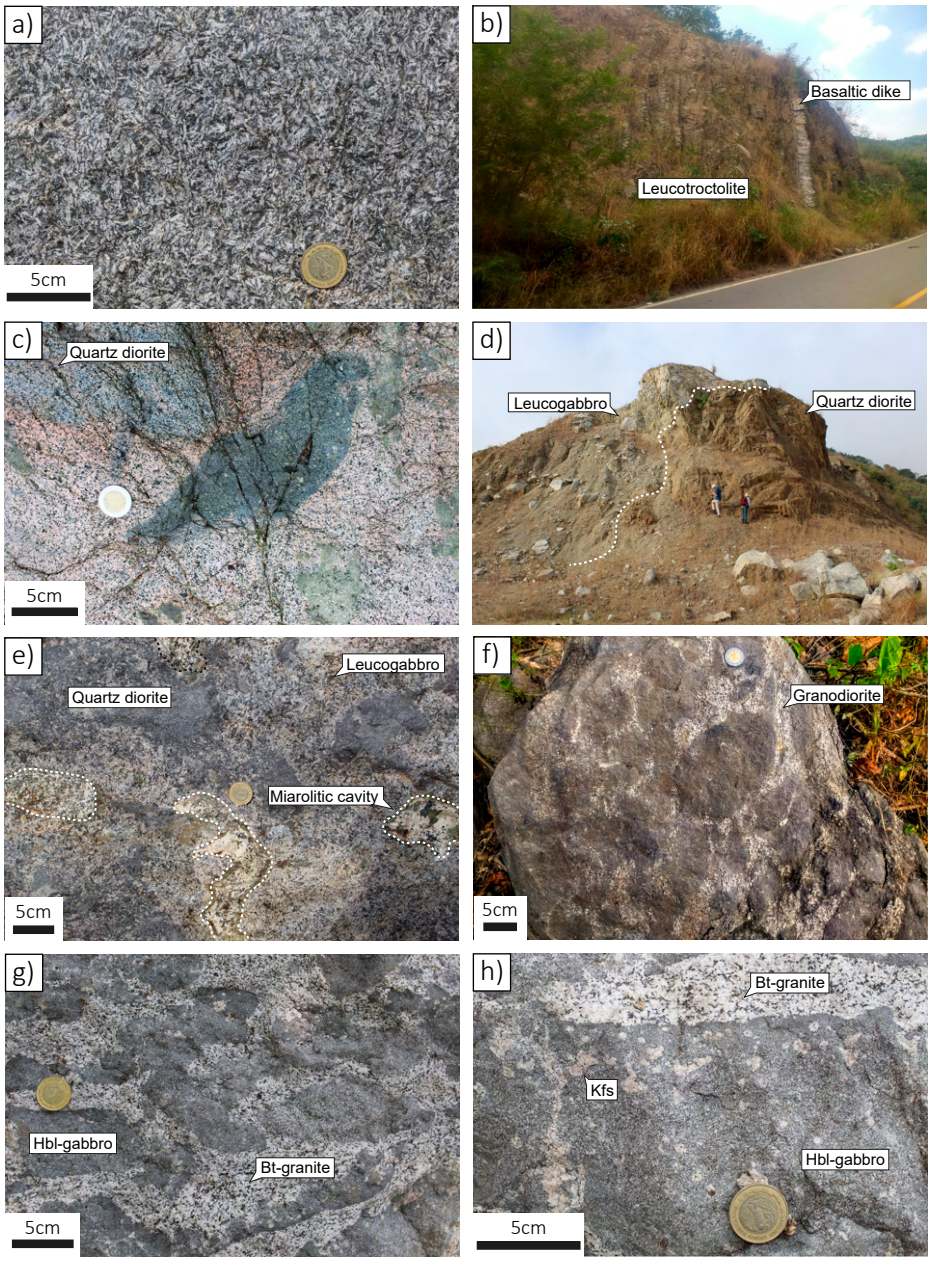

Figure 2. Outcrop photographs of LHPC field relationships. a) Leucogabbro sample with holocrystalline texture observed near La Huerta town. b) Leucotroctolites intercalated with basaltic dikes from the gabbroic bodies near Juan Gil Preciado town. c) Dioritic enclaves in the Cuitzmala granitic pluton. d) Intrusive contact between leucogabbros and the quartz-dioritic chilled margin of the Cuitzmala pluton. e) Patches of leucogabbros and quartz-diorites and miarolitic cavities in the border of the Cuitzmala pluton. f) Schollen texture with ovoid-shaped dioritic enclaves supported by a granodioritic melt from the Los Cimientos pluton. g) Cuspate contacts of Hbl-gabbro enclaves floating in a Bt-granite from El Totole pluton. h) Kfs crystals in the border between Hbl-gabbro and Bt-granite in El Totole pluton.

opx, and cpx rimmed by amphibole (Figure 3a) and a second type of amphibole occurs as interstitial fibrous crystals. In some cases, pyroxene shows poikilitic textures with large plagioclase inclusions. Accessory phases are magnetite and ilmenite partially replaced by titanite. The associated leucotroctolites are composed of a fine-grained mosaic of Ca-rich plagioclase forming an ophitic texture. The interstitial phases are anhedral opx-rimmed olivine, reddish-brown biotite (Figure 3b) and symplectites of opx and plagioclase as peritectic phases (Figure 3c). The gabbroic rocks at the northwestern edge of the Los Cimientos hybrid pluton have >60 % Ca-rich plagioclase with interstitial olivine rimmed by brown amphibole (Figure 3d).

Granitic-granodioritic rocks

Granitic rocks are generally composed of plagioclase (36–45 %), K feldspar (24–40 %), and quartz (18–26 %) with minor biotite (2–6 %) and amphibole (0.1–14 %). The monzogranitic core of the Cuitzmala pluton contains minor inclusions of amphibole in biotite (<0.1 %). The syenogranitic borders of the pluton exhibit large K feldspar crystals rimmed by graphic textures of quartz and plagioclase. Chilled margins of the El Chico pluton are quartz-dioritic to dioritic with anti-rapakivi textures with cpx inclusions in the plagioclase cores (Figure 3e) as well as opx crystals rimmed by greenish-brown amphibole. Biotite in El Chico quartz-diorites is partially replaced by amphibole.

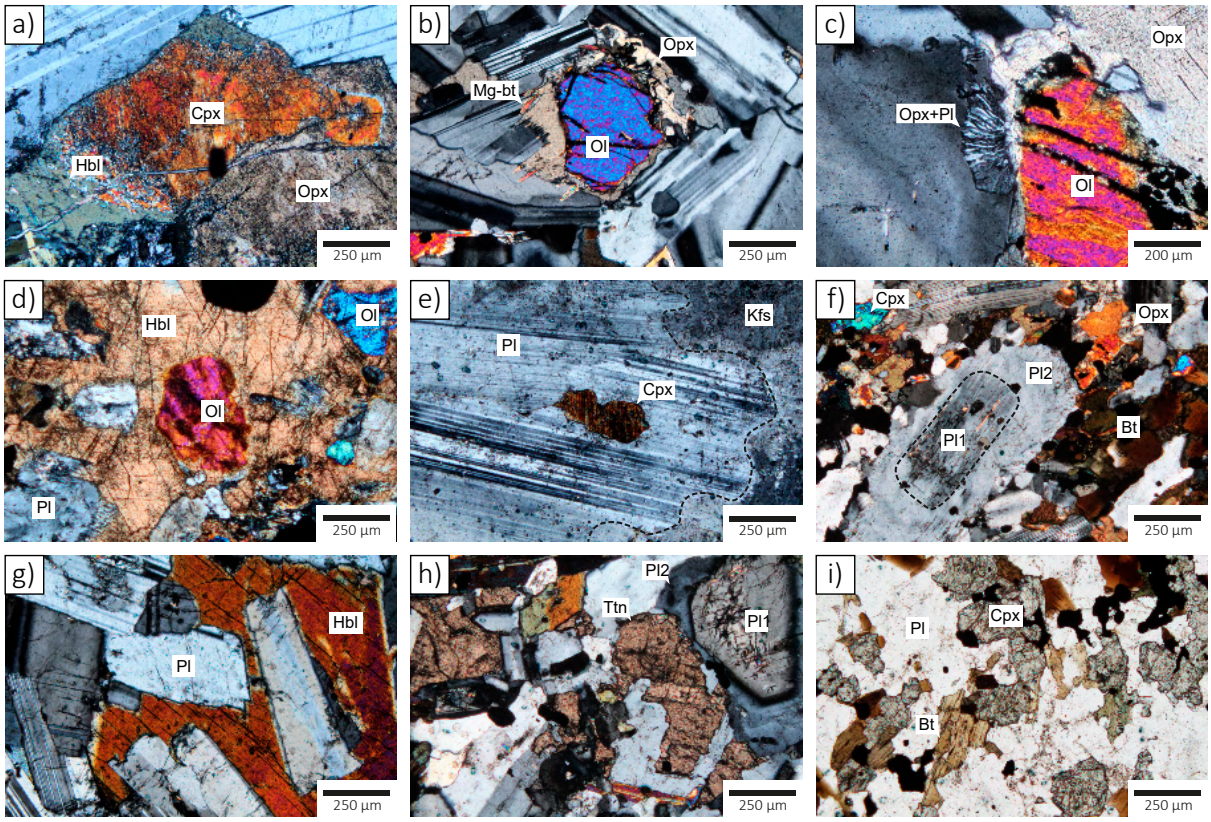

Figure 3. Photomicrographs from the LHPC. a) Interstitial orthopyroxene and clinopyroxene in leucogabbros, partially replaced by hornblende. b) Leucotroctolite with interstitial olivine, rim around the olivine crystal is composed of orthopyroxene and phlogopite. c) Symplectitic growth between orthopyroxene and plagioclase. d) Gabbroic rock from Los Cimientos with hornblende surrounding olivine. e) El Chico quartz-diorite with antirapakivi texture and clinopyroxene inclusions within the plagioclase core. f) Hybrid quartz-diorite from the chilled margin of the Cuitzmala pluton, with two plagioclase growth stages, orthopyroxene, clinopyroxene, and biotite. g) Hornblende gabbro with ophitic texture and interstitial hornblende. h) Hybrid hornblende gabbro with the development of titanite in place of hornblende, interstitial quartz, and plagioclase with two growth stages. i) Los Cimientos quartz-diorite with clinopyroxene crystals solvated by biotite crystals.

The chilled margin of the Cuitzmala pluton in contact with the La Huerta gabbros commonly shows partly hybridized textures, characterized by the presence of cpx and opx, red biotite and zoned plagioclase resembling the leucogabbros and leucotroctolite assemblages (Figure 3f).

Granites and granodiorites from the Cihuatlán pluton are composed of quartz, plagioclase, and K feldspar with minor amount of amphibole and biotite. Plagioclase forms clots of two or more crystals with honeycomb-like textures in their cores. On the other hand, the contained MMEs are mostly plagioclase, amphibole, and biotite with interstitial quartz and titanite; in turn amphibole is rimmed by opaque minerals.

Quartz-dioritic to gabbroic hybrid rocks

The mafic member of the hybrid plutons is composed of hornblende-gabbros with Ca-rich plagioclase (55–75 vol. %), variable amounts of brown amphibole, and minor contents of biotite, titanite, and interstitial quartz with cummulitic or ophitic textures (Figure 3g). K feldspar remains as an interstitial phase probably related to a late magmatic stage.

Hybrid quartz-diorites have 50–65 vol.% zoned plagioclase (Figure 3h) with labradorite rimmed by andesine. The cores are rich in magnetite inclusions and anhedral cpx. As in other gabbroic rocks, plagioclase crystals appear to be oriented along a magmatic foliation and sometimes form pseudo-cummulitic textures with interstitial cpx, opx, biotite, magnetite, quartz, and K feldspar. Opx and cpx resemble crystals from gabbroic rocks, whereas biotite and amphibole show similar optical characteristics as those of the granitic rocks (Figure 3i).

Mineral chemistry

The chemical composition of amphibole, biotite, olivine, plagioclase, and pyroxene from the LHPC samples are listed in Table 1 and plotted in compositional diagrams according to their lithological units (Figure 4). Analytical details are given in Supplementary File 1.

Amphibole (~0.1–25 vol. %) occurs as a secondary phase in gabbroic rocks and as primary phenocrysts in all other LHPC intrusives. Based on the $^{A}(Na+K+2Ca)$ and $^{C}(Al+Fe^{+3}+2Ti)$ atoms per formula unit (a.p.f.u.; Hawthorne *et al.,* 2012), most amphiboles are classified as Mg-hornblende and follow two arrays: crystals from gabbroic rocks show A cations ranging from 0.1 to 0.6 and C cations from 0.5 to 1.5, whereas crystals from granitic rocks display C cations <1.0 and A cations from 0.2 to 0.6 (Figure 4a). Amphiboles rimming pyroxene in gabbros are predominantly Mg-hornblende, whereas fibrous shaped amphiboles show pargasitic composition. This array forms a mixing line between the two types (Figure 4a). Amphiboles of granitic rocks are mostly alkaline Mg-hornblende, but in hybrid and chilled margin rocks, they are pargasitic.

Biotite is a common phase in all LHPC units (~0.3–18 vol. %) with a wide range of compositions depending on the lithology (Figure 4b). Biotite exhibit X_{Mg} ($Mg/Mg+Fe^{2+}$) ranging from 0.35 to 0.73 and Ti (apfu) from 0.16 to 0.29 (Figure 4b). Brown crystals from granitic and hybrid rocks are chemically similar and plot in the biotite field.

Table 1. Representative mineral chemistry analyses of LHPC rocks. Number of cations was calculated on the basis of 23 oxygens (amphibole), 22 oxygens (biotite), 6 oxygens (pyroxenes), 4 oxygens (olivine), 8 oxygens (plagioclase). Amphiboles were classified according to Hawthorne *et al.* (2012) by the algorithm of Locock (2014). Ferric iron is calculated by charge balance. Abbreviations: XMg = Mg/(Mg + Fe); XAn = Ca/(Na+Ca+K); XAb = Na/(Na+Ca+K); XOr = K/(Na+Ca+K).

Amphibole					**Biotite**					**Clinopyroxene**					**Ortho-pyroxene**	**Olivine**		**Plagioclase cores**					**Plagioclase rims**			
	Gabbroic rocks	Quartz-dioritic to gabbroic hybrid rocks	Quartz-dioritic chilled margins	Granitic to grano-dioritic rocks		Gabbroic rocks	Quartz-dioritic to gabbroic hybrid rocks	Quartz-dioritic chilled margins	Granitic to grano-dioritic rocks		Gabbroic rocks	Quartz-dioritic to gabbroic hybrid rocks	Quartz-dioritic chilled margins	Quartz-dioritic chilled margins (inclusions in pl)	Gabbroic rocks		Gabbroic rocks		Gabbroic rocks	Quartz-dioritic to gabbroic hybrid rocks	Quartz-dioritic chilled margins	Granitic to grano-dioritic rocks	Gabbroic rocks	Quartz-dioritic to gabbroic hybrid rocks	Granitic to grano-dioritic rocks	Quartz-dioritic chilled margins
	Panseri (2007)	LUP	LUP	LUP		LUP	LUP	LUP	LUP		LUP	LUP	LUP	LUP	LUP		LUP		Panseri (2007)	LUP	LUP	LUP	Panseri (2007)	LUP	LUP	LUP
SiO_2	44.75	47.80	46.67	48.05	SiO_2	38.82	36.66	40.46	36.70	SiO_2	48.74	51.35	49.87	47.04	51.68	SiO_2	35.54	SiO_2	53.44	49.80	63.65	61.13	66.37	59.58	67.16	64.51
TiO_2	0.70	1.36	1.43	1.01	TiO_2	4.09	4.09	5.01	3.67	TiO_2	1.10	0.12	0.25	1.34	0.36	TiO^2	0.01	TiO_2	0.00	0.04	0.05	0.01		0.03	0.00	0.01
Al_2O_3	10.41	6.49	5.78	5.59	Al_2O_3	16.17	14.18	13.00	14.65	Al_2O_3	2.68	0.70	1.46	6.20	0.77	Al_2O_3	0.01	Al_2O_3	30.65	32.21	25.22	25.79	22.16	25.51	18.91	23.61
FeO_T	-	15.92	20.11	18.12	FeO_T	11.63	19.01	13.52	20.99	FeO_T	10.66	9.25	10.86	21.83	22.51	Cr_2O_3	0.00	FeO_T	0.00	0.26	0.13	0.08	0.00	0.55	0.08	0.17
Fe_2O_3	7.52	-	-	-	Fe_2O_3	-	-	-	-	Fe_2O_3	-	-	-	-	-	Fe_2O_3	-	Fe_2O_3	-	-	-	-	-	-	-	-
FeO	12.37	-	-	-	FeO	-	-	-	-	FeO	-	-	-	-	-	FeO	-	FeO	-	-	-	-	-	-	-	-
MnO	0.46	0.38	0.43	0.97	MnO	0.06	0.30	0.11	0.87	MnO	0.27	0.74	0.48	0.48	0.53	FeO_T	38.00	MnO	-	-	0.02	0.01	0.00	0.00	0.03	0.01
MgO	9.57	13.08	10.43	12.34	MgO	13.77	12.21	16.25	10.06	MgO	15.40	14.24	15.60	8.71	21.75	MnO	0.63	MgO	-	-	0.00	0.04	0.00	0.00	0.00	0.01
CaO	11.29	12.23	10.96	10.48	CaO	3.78	0.15	0.04	0.02	CaO	21.38	23.36	20.93	11.35	1.45	MgO	26.16	CaO	11.89	15.66	6.42	6.77	1.76	7.70	0.09	4.85
Na_2O	1.38	0.91	1.52	1.60	Na_2O	0.18	0.06	0.14	0.09	Na_2O	0.44	0.33	0.38	1.58	0.04	CaO	0.18	Na_2O	4.56	2.69	7.73	7.14	10.75	7.16	1.04	8.83
K_2O	0.28	0.64	0.85	0.30	K_2O	7.93	9.54	9.08	9.48	K_2O	0.02	0.03	0.02	0.77	0.03	NiO	0.02	K_2O	0.00	0.08	0.66	0.28	0.00	0.31	16.85	0.35
TOTAL	98.73	98.80	98.17	98.46	TOTAL	96.41	96.18	97.60	96.52	TOTAL	100.67	100.12	99.85	99.30	99.12	TOTAL	100.55	TOTAL	100.54	100.73	103.87	101.24	101.04	100.84	104.17	102.36
Site T																										
Si	6.86	6.96	7.02	7.08	**Site T**					**Site T**						**Site T**		**Site T**								
Ti	0.09	-	-	-	Si	2.98	2.83	2.98	2.85	Si	1.84	1.94	1.89	1.85	1.93	Si	1.00	Si	2.40	2.26	2.72	2.68	2.88	2.64	2.99	2.79
Al	1.05	1.04	0.98	0.92	Al	1.02	1.17	1.02	1.15	Al	0.12	0.03	0.07	0.15	0.04	**Site M**		Al	1.62	1.72	1.27	1.33	1.13	1.33	0.99	1.20
Site C					**Site M**					Ti	0.03	0.00	0.01	0.04	0.01	Mg	1.09	**Site M**								
Ti	0.08	0.15	0.16	0.11	Al	0.44	0.11	0.10	0.20	**Site M1**						Fe^{+2}	0.89	Fe^{+2}	-	0.01	0.00	0.00	0.00	0.02	0.00	0.01
Al	-	0.07	0.04	0.05	Fe^{+2}	0.75	1.23	0.83	1.36	Al	0.00	0.00	0.00	0.13	0.00	Fe^{+3}	0.00	Mn	-	-	-	-	-	-	-	-
Fe^{+2}	2.17	1.54	2.23	1.74	Mn	0.00	0.02	0.01	0.06	Fe^{+3}	0.26	0.17	0.25	0.15	0.13	Ca	0.01	Mg	-	-	-	-	-	-	-	-
Fe^{+3}	0.47	0.40	0.22	0.39	Mg	1.57	1.40	1.78	1.17	Fe^{+2}	0.06	0.12	0.09	0.56	0.57	Mn	0.01	Ca	0.57	0.76	0.29	0.32	0.08	0.37	0.00	0.22
Mg	2.27	2.84	2.34	2.71	Ti	0.24	0.24	0.28	0.21	Mn	0.01	0.02	0.02	0.02	0.02	Ni	0.00	Na	0.40	0.24	0.65	0.62	0.92	0.62	0.09	0.75
Site B					**Site A**					Mg	0.76	0.77	0.76	0.14	0.34	Al	0.00	K	0.00	0.00	0.04	0.02	0.00	0.02	0.96	0.02
Mn	0.05	0.04	0.06	0.12	K	0.78	0.94	0.85	0.94	**Site M2**						Cr	0.00									
Fe^{+2}	0.07	-	0.07	0.10	Ca	0.31	0.01	0.00	0.00	Mg	0.10	0.03	0.12	0.36	0.94	Ti	0.00	X_{An}	0.59	0.76	0.30	0.33	0.08	0.36	0.00	0.23
Ca	1.73	1.91	1.77	1.65	Na	0.03	0.01	0.02	0.01	Ca	0.86	0.94	0.85	0.48	0.06			X_{Ab}	0.41	0.24	0.66	0.65	0.92	0.62	0.09	0.75
Na	0.14	0.26	0.11	0.12						Na	0.03	0.02	0.03	0.12	0.00	X_{Mg}	0.55	X_{Or}	0.00	0.00	0.04	0.02	0.00	0.02	0.91	0.02
Site A					X_{Mg}	0.68	0.53	0.68	0.46	K	0.00	0.00	0.00	0.04	0.00	Fo	0.55									
Na	0.37	0.21	0.34	0.33												Fa	0.45									
K	0.18	0.12	0.16	0.06						X_{Mg}	0.93	0.87	0.91	0.48	0.69											

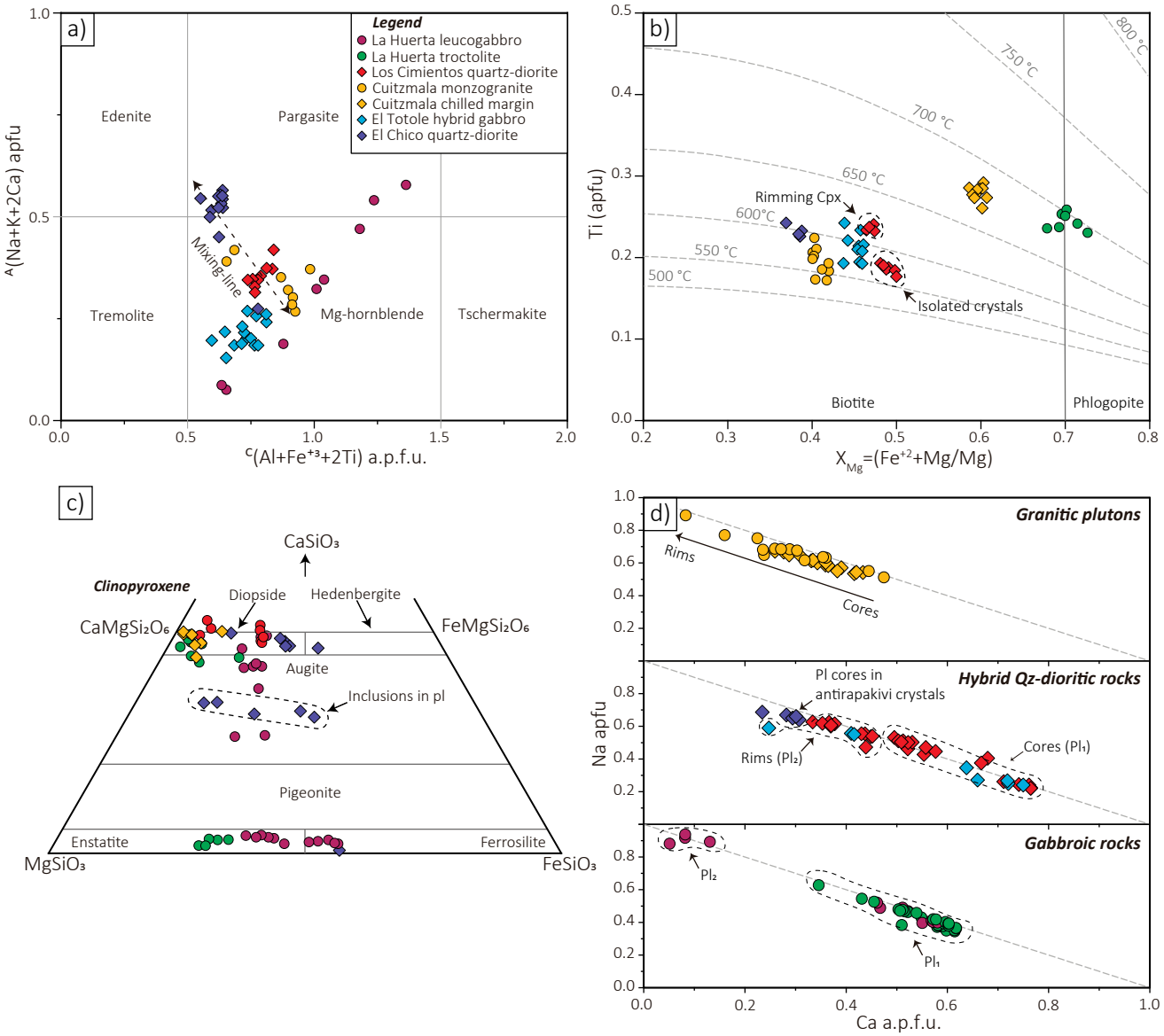

Figure 4. Mineral chemistry plots of LHPC rocks. a) amphiboles (Hawthorne *et al.*, 2012), b) biotites (Foster, 1960) with the temperature curves estimated by Henry (2005), c) pyroxenes ($CaSiO_3$-$MgSiO_3$-$FeSiO_3$), d) plagioclase (Ca-Na a.p.f.u.).

Reddish-brown crystals from leucotroctolites and chilled margins of granitic plutons are considered Mg-biotites due to their high values of Mg (X_{Mg} 0.67–0.73) and Ti (0.24–0.29 a.p.f.u.) and classify close to the phlogopite field. Biotite crystals rimming cpx are more enriched in Ti than isolated crystals in the matrix. Cpx (~1.5–13.5 vol. %) and opx (~4.0–22.8 vol. %) have very low content of Al^{IV} (<0.1 a.p.f.u.) and other octahedral cations such as Ti, Cr, or Mn. Cpx show diopside compositions with X_{Mg} ranging from 0.66 to 0.97 and opx are enstatites to ferrosilites with X_{Mg} from 0.65 to 0.71 (Figure 4c). Cpx inclusions in plagioclase display an augitic composition with X_{Mg} from 0.46 to 0.79 (Figure 4c).

Olivine crystals in leucotroctolites (~13–17 vol. %) lack chemical zoning and show relatively high-Fe compositions of Fo_{60-56} Fa_{45-39} and X_{Mg} from 0.55 to 0.60 (Table 1).

Plagioclase is the most abundant phase in the LHPC rocks (~31–78 vol. %) and displays a wide range of compositions depending on the lithology (Figure 4d). In gabbroic rocks, its content is between 51 and 73 vol. % and it is characterized by chemically homogenous crystals of An_{59-51} and secondary plagioclase with An_8. In granitic rocks, plagioclase (~31–56 vol. %) shows strong chemical zoning with an increase in albite from 65% at the core to 75 % at the rim. Antirapakivi textures in the chilled margins of these bodies are formed by plagioclase cores (An_{35-30} Ab_{60-66} Or_{4-7}) rimmed by K feldspar of Or_{91} Ab_9 (Figure 4d). The gabbroic portion from hybrid plutons contains plagioclase cores (50–78 vol. %) with An_{75-70} Ab_{25-30} rimmed by more albitic compositions ($An_{42-28}Ab_{57-68}$). In the hybrid quartz-diorites, plagioclase shows strong normal zonation of labradoritic composition (Pl_1) from $An_{77-75}Ab_{23-25}$ to andesine rims (Pl_2) of $An_{37-34}Ab_{61-63}$ (Figure 4d).

Geochemistry and Sr-Nd isotopes

Mayor and trace element geochemistry

Thirteen samples from the main LHPC plutonic bodies were analyzed for major and trace element concentrations by XRF and ICP-MS analyses, respectively. Additionally, major element concentrations from three Cihuatlán pluton samples are provided (Schaaf, 1990; Schaaf *et al.* 2022). All data are compiled in Table 2. Major and trace element

Table 2. Major and trace element geochemical analyses of representative LHPC rocks. The concentration of major and trace elements of LHPC rocks in wt. % and ppm, respectively. Analytical details can be consulted in Supplementary File 1. Data obtained at Laboratorio Universitario de Petrologia, UNAM (LUP).

	PVA19-2	**PVA19-3**	**PVA19-5**	**PVA19-7**	**PVA19-9a**	**PVA19-11**	**PVA19-13**	**PVA19-15**	**PVA19-17a**	**PVA19-18a**	**PVA19-22**	**PVA19-24**	**PVA19-25**	**MS18a**	**MS18b**	**MS19**
Laboratory	ACT	ACT	LANGEM	LANGEM	LANGEM	LANGEM	LANGEM	LANGEM	LANGEM	LANGEM	LANGEM	LANGEM	LANGEM	Schaaf, 1990	Schaaf, 1990	Schaaf, 1990
Typology	Gabbroic rocks	Gabbroic rocks	Gabbroic rocks	Quartz-dioritic chilled margins	Quartz-diori-tic to gabbroic hybrid rocks	Quartz-dioritic chilled margins	Granitic to granodioritic rocks	Granitic to granodioritic rocks	Gabbroic rocks	Gabbroic rocks	Granitic to granodioritic rocks	Quartz-diori-tic to gabbroic hybrid rocks	Gabbroic rocks	Granitic to granodioritic rocks	Granitic to granodioritic rocks	Granitic to granodioritic rocks
Petrographic classification	Leucogabbro	Leucotroctolite	Leucogabbro	Hybrid quartz-diorite	Hybrid horn-blende gabbro	Quartz-diorite	Monzogranite	Monzogranite	Leucogabbro	Leucotroctolite	Monzogranite	Hybrid quartz-diorite	Leucogabbro	Granodiorite	Quartz-diorite	Granite
Pluton	La Huerta gabbroic body	La Huerta gab-broic body	La Huerta gab-broic body	Cuitzmala pluton	El Totole pluton	El Chico pluton	Cuitzmala pluton	Cuitzmala pluton	La Huerta gab-broic body	La Huerta gab-broic body	Cuitzmala pluton	Los Cimientos pluton	La Huerta gab-broic body	Cihuatlán pluton	Cihuatlán pluton	Cihuatlán pluton
X	534649	536296	536162	536049	541669	546014	526690	518148	492931	493493	505919	518450	510532	539885	539885	547672
Y	2150267	2152858	2151146	2144177	2153366	2163476	2158095	2165640	2168280	2168766	2166543	2178406	2184011	2124845	2124845	2128122
(wt%)																
SiO_2	46.45	50.16	46.13	60.37	53.91	60.81	74.08	73.13	47.58	48.51	74.31	53.22	45.60	68.50	56.90	76.65
TiO_2	2.09	0.97	1.35	1.01	1.11	1.17	0.21	0.25	1.97	0.70	0.22	1.45	1.64	0.46	1.01	0.20
Al_2O_3	18.03	18.81	19.91	16.23	17.64	15.95	13.75	14.14	17.68	20.77	13.63	16.31	16.13	14.99	16.88	13.23
Fe_2O_3 t	13.23	9.53	11.25	6.72	9.98	6.74	1.83	2.10	12.59	10.49	1.55	11.38	14.28	1.82	4.11	0.79
FeO	-	-	-	-	-	-	-	-	-	-	-	-	-	1.44	2.89	0.55
MnO	0.19	0.16	0.20	0.11	0.16	0.11	0.06	0.07	0.17	0.13	0.06	0.18	0.16	0.09	0.19	0.07
MgO	4.92	6.33	4.92	2.58	3.97	2.03	0.43	0.56	4.41	6.64	0.45	4.07	6.56	1.40	3.45	0.35
CaO	10.83	10.55	12.02	5.34	6.95	4.50	1.57	1.94	9.10	8.89	1.36	7.81	10.35	3.20	5.32	1.29
Na_2O	2.93	3.09	2.12	3.68	3.77	3.93	4.00	4.15	4.09	3.27	4.03	3.59	2.80	4.05	4.12	3.81
K_2O	0.44	0.55	0.75	3.31	1.53	4.09	3.49	3.27	0.61	0.67	3.75	1.55	1.21	3.17	2.12	3.76
P_2O_5	0.06	0.15	0.10	0.28	0.33	0.34	0.05	0.07	0.17	0.18	0.05	0.32	0.07	0.13	0.38	0.06
LOI	1.32	0.29	1.27	0.38	0.66	0.34	0.53	0.32	1.65	-0.24	0.61	0.12	1.21	-	-	-
Total	100.50	100.60	100.00	100.00	100.00	100.00	100.00	100.00	100.00	100.00	100.00	100.00	100.00	99.71	97.88	100.76
(ppm)																
B	-	-	12.23	7.66	10.34	16.43	5.10	6.27	7.06	6.08	8.65	6.64	9.24	-	-	-
P	-	-	0.11	0.27	0.34	0.34	0.06	0.08	0.16	0.20	0.06	0.29	0.08	-	-	-
Ti	-	-	1.31	1.03	1.08	1.12	0.22	0.27	1.95	0.72	0.22	1.32	1.55	-	-	-
Li	-	-	11.24	18.82	19.48	8.96	13.57	22.10	20.61	7.68	14.29	13.67	5.66	-	-	-
Sc	36.00	28.00	30.19	16.51	17.01	19.88	2.45	5.66	38.56	7.43	4.06	28.12	41.52	-	-	-
Be	<1	<1	0.60	2.11	1.20	2.88	1.61	1.74	0.85	0.84	1.77	1.19	0.73	-	-	-
V	532.00	227.00	348.52	125.67	184.23	109.36	10.68	14.56	567.20	102.14	11.09	252.05	425.21	-	-	-
Cr	120.00	120.00	95.57	88.42	66.50	111.20	160.05	151.54	43.59	92.00	155.77	72.43	39.95	-	-	-
Co	39.00	36.00	43.47	15.55	26.00	13.00	2.26	2.73	38.06	50.86	2.32	26.62	51.15	-	-	-
Ni	60.00	60.00	15.22	16.08	9.05	8.91	2.37	2.39	26.62	72.95	2.76	11.81	18.67	-	-	-
Cu	40.00	60.00	74.71	79.81	61.42	13.32	0.69	1.24	332.48	57.63	11.80	68.25	120.63	-	-	-
Zn	110.00	80.00	103.68	65.94	83.29	52.58	24.29	30.74	116.01	74.24	14.59	98.94	122.77	-	-	-
Ga	20.00	18.00	19.46	18.77	18.60	19.30	13.56	14.51	20.31	18.86	15.01	18.54	18.54	-	-	-
Ge	1.30	1.30	-	-	-	-	-	-	-	-	-	-	-	-	-	-
As	<5	<5	-	-	-	-	-	-	-	-	-	-	-	-	-	-

continues

Table 2 (continued). Major and trace element geochemical analyses of representative LHPC rocks. The concentration of major and trace elements of LHPC rocks in wt. % and ppm, respectively. Analytical details can be consulted in Supplementary File 1. Data obtained at Laboratorio Universitario de Petrologia, UNAM (LUP).

	PVA19-2	**PVA19-3**	**PVA19-5**	**PVA19-7**	**PVA19-9a**	**PVA19-11**	**PVA19-13**	**PVA19-15**	**PVA19-17a**	**PVA19-18a**	**PVA19-22**	**PVA19-24**	**PVA19-25**	**MS18a**	**MS18b**	**MS19**
Laboratory	ACT	ACT	LANGEM	LANGEM	LANGEM	LANGEM	LANGEM	LANGEM	LANGEM	LANGEM	LANGEM	LANGEM	LANGEM	Schaaf, 1990	Schaaf, 1990	Schaaf, 1990
Typology	Gabbroic rocks	Gabbroic rocks	Gabbroic rocks	Quartz-dioritic chilled margins	Quartz-dioritic to gabbroic hybrid rocks	Quartz-dioritic chilled margins	Granitic to granodioritic rocks	Granitic to granodioritic rocks	Gabbroic rocks	Gabbroic rocks	Granitic to granodioritic rocks	Quartz-dioritic to gabbroic hybrid rocks	Gabbroic rocks	Granitic to granodioritic rocks	Granitic to granodioritic rocks	Granitic to granodioritic rocks
Petrographic classification	Leucogabbro	Leucotroctolite	Leucogabbro	Hybrid quartz-diorite	Hybrid hornblende gabbro	Quartz-diorite	Monzogranite	Monzogranite	Leucogabbro	Leucotroctolite	Monzogranite	Hybrid quartz-diorite	Leucogabbro	Granodiorite	Quartz-diorite	Granite
Pluton	La Huerta gabbroic body	La Huerta gabbroic body	La Huerta gabbroic body	Cuitzmala pluton	El Totole pluton	El Chico pluton	Cuitzmala pluton	Cuitzmala pluton	La Huerta gabbroic body	La Huerta gabbroic body	Cuitzmala pluton	Los Cimientos pluton	La Huerta gabbroic body	Cihuatlán pluton	Cihuatlán pluton	Cihuatlán pluton
X	534649	536296	536162	536049	541669	546014	526690	518148	492931	493493	505919	518450	510532	539885	539885	547672
Y	2150267	2152858	2151146	2144177	2153366	2163476	2158095	2165640	2168280	2168766	2166543	2178406	2184011	2124845	2124845	2128122
Rb	8.00	8.00	19.94	99.26	36.19	131.18	84.79	90.69	12.25	13.43	97.93	43.75	32.16	-	-	-
Sr	598.00	526.00	690.74	378.86	486.63	328.08	168.05	183.58	493.75	539.56	161.25	423.92	618.70	-	-	-
Y	11.50	16.10	11.28	30.17	24.32	35.56	12.52	14.87	19.48	12.25	13.37	27.17	15.76	-	-	-
Zr	35.00	66.00	45.59	296.25	134.86	313.57	96.71	108.16	137.37	76.09	109.16	82.95	56.04	-	-	-
Nb	1.70	2.80	2.70	15.66	6.00	19.77	7.08	8.21	4.43	4.22	8.22	7.29	2.84	-	-	-
Mo	<2	<2	1.08	1.31	0.97	2.75	1.29	1.47	1.01	1.26	3.64	1.71	1.21	-	-	-
Ag	<0.5	<0.5	-	-	-	-	-	-	-	-	-	-	-	-	-	-
In	<0.1	<0.1	-	-	-	-	-	-	-	-	-	-	-	-	-	-
Sn	<1	<1	0.86	1.80	1.05	2.47	1.35	1.02	0.83	0.67	0.90	1.24	0.94	-	-	-
Sb	<0.2	<0.2	1.29	0.21	0.22	0.39	0.10	0.12	0.11	0.08	0.08	0.17	0.64	-	-	-
Cs	0.20	0.40	0.52	2.57	0.76	2.12	1.32	1.67	9.47	1.14	0.77	0.95	1.44	-	-	-
Ba	201.00	235.00	259.72	684.60	491.76	745.17	985.07	778.78	365.37	295.31	883.09	397.80	319.88	-	-	-
La	4.34	7.27	5.68	24.27	13.51	29.43	17.02	17.13	7.77	8.39	19.36	14.73	6.24	-	-	-
Ce	10.00	16.70	13.00	48.12	30.46	62.40	30.60	31.51	18.15	18.95	36.29	33.07	14.92	-	-	-
Pr	1.44	2.33	1.76	6.32	4.12	8.13	3.26	3.42	2.53	2.48	3.95	4.48	2.09	-	-	-
Nd	7.00	10.80	8.39	25.52	18.33	32.77	11.52	12.31	12.16	11.06	13.88	19.95	10.27	-	-	-
Sm	1.94	2.80	2.16	5.68	4.49	7.31	2.19	2.38	3.30	2.60	2.57	5.01	2.91	-	-	-
Eu	1.05	1.05	0.86	1.33	1.40	1.46	0.62	0.64	1.23	1.01	0.57	1.42	0.93	-	-	-
Gd	2.31	2.95	2.22	5.25	4.37	6.56	1.98	2.20	3.45	2.50	2.21	4.93	3.06	-	-	-
Tb	0.37	0.47	0.35	0.83	0.69	1.05	0.32	0.37	0.56	0.38	0.36	0.79	0.49	-	-	-
Dy	2.23	2.90	2.14	4.80	4.13	5.99	1.98	2.28	3.43	2.27	2.13	4.73	2.98	-	-	-
Ho	0.42	0.57	0.43	0.95	0.82	1.16	0.43	0.50	0.69	0.46	0.46	0.92	0.59	-	-	-
Er	1.20	1.67	1.15	2.68	2.31	3.33	1.25	1.49	1.90	1.24	1.35	2.57	1.56	-	-	-
Tm	0.17	0.24	-	-	-	-	-	-	-	-	-	-	-	-	-	-
Yb	1.04	1.55	1.07	2.64	2.30	3.35	1.44	1.78	1.85	1.17	1.59	2.44	1.42	-	-	-
Lu	0.17	0.24	0.16	0.40	0.35	0.51	0.23	0.29	0.28	0.18	0.25	0.36	0.21	-	-	-
Hf	0.90	1.40	1.10	6.83	3.19	7.23	2.72	3.01	3.12	1.75	3.12	2.07	1.46	-	-	-
Ta	0.12	0.17	0.16	1.07	0.38	1.35	0.69	0.84	0.27	0.25	0.78	0.42	0.18	-	-	-
W	1.20	<0.5	0.75	1.33	0.67	0.95	0.48	0.68	0.83	0.46	0.78	0.64	1.16	-	-	-
Tl	<0.05	<0.05	0.11	0.30	0.14	0.28	0.39	0.34	0.04	0.02	0.36	0.15	0.14	-	-	-
Pb	5.00	<5	8.39	7.83	3.42	7.71	9.94	9.32	3.67	3.36	9.76	4.55	7.81	-	-	-
Bi	<0.1	<0.1	-	-	-	-	-	-	-	-	-	-	-	-	-	-
Th	0.36	0.48	0.81	8.66	2.04	15.20	7.28	7.47	0.81	0.85	7.96	2.13	2.10	-	-	-
U	0.13	0.20	0.26	2.90	0.93	5.95	1.72	2.10	0.42	0.28	2.08	0.77	0.78	-	-	-

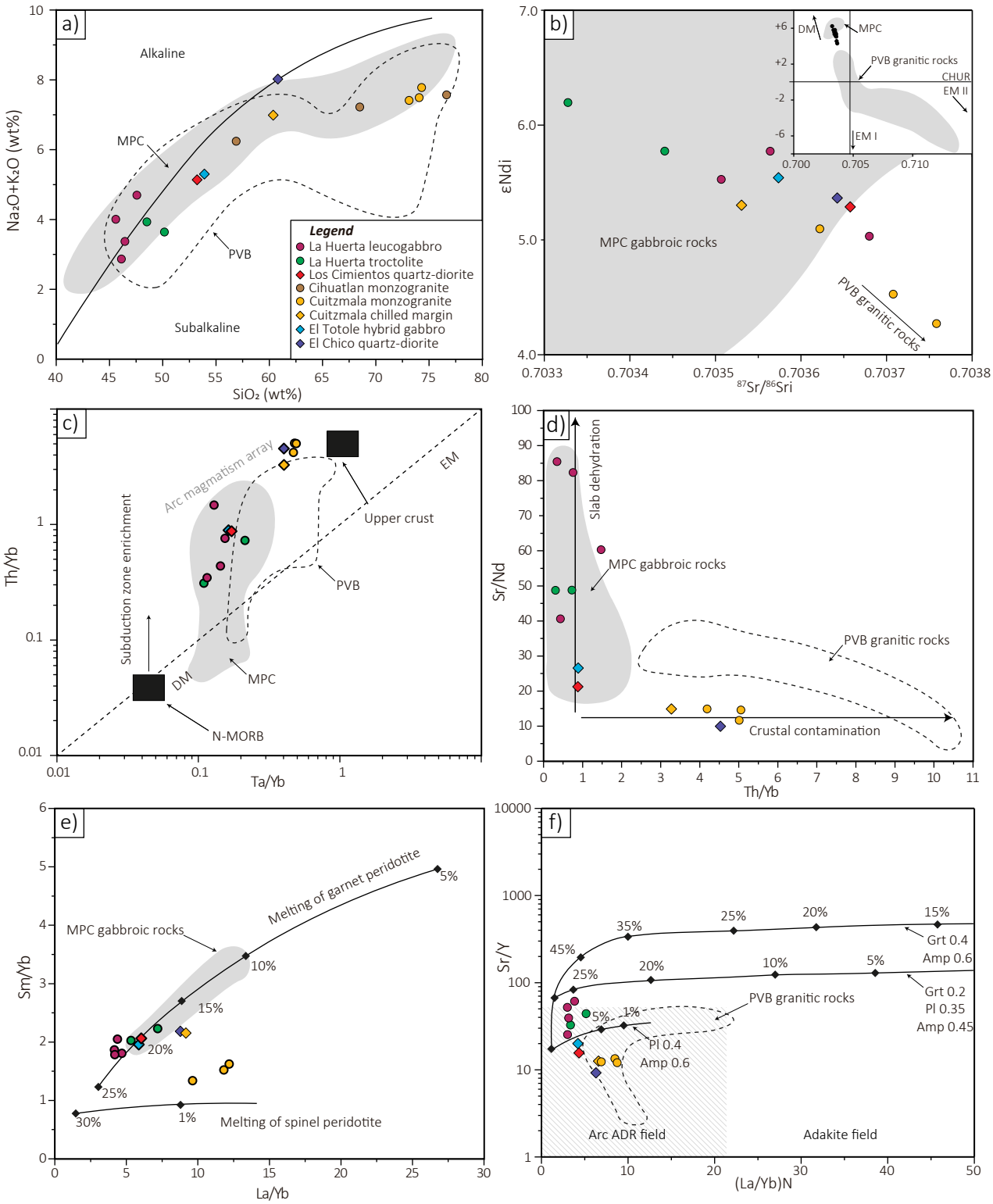

Figure 5. Geochemical classification diagrams based on major and trace elements of LHPC rocks. The range of MPC rocks is shown in gray (Panseri, 2007; Schaaf *et al.*, 2022), the area enclosed in the dashed line corresponds to the compositional range of PVB rocks (Schaaf *et al.*, 2020; Valencia *et al.*, 2013). a) SiO_2 *vs.* alkalis diagram. b) Initial εNd *vs.* $^{87}Sr/^{86}Sr$ values for LHPC rocks. Data for MPC rocks are from Panseri (2007) and Schaaf *et al.* (2022). Additionally, the inset shows the field for PVB granitic rocks (Schaaf *et al.*, 2020). c) Th/Yb *vs.* Ta/Yb discrimination processes diagram after Pearce (1983). d) Discrimination processes diagram (after Woodhead *et al.*, 1998) based on Sr/Nd *vs.* Th/Yb. e) Sm/Yb *vs.* La/Yb diagram showing melting curves of garnet peridotite and spinel peridotite (after Johnson *et al.*, 1990). f) Sr/Y *vs.* $(La/Yb)_N$ diagram with melting curves for granulitic sources (after Triantafyllou *et al.*, 2020) and the fields for adakitic and arc andesitic-dacitic rocks (ADR).

compositions match the general trend of the neighboring MPC and PVB (*e.g.* Figure 5a); most of the studied samples show subalkaline composition, whereas four gabbroic and hybrid rocks plot in or at the border of the subalkaline field (Figure 5a). According to the Frost and Frost (2008) Aluminum Saturation Index (ASI), most of the samples are classified as metaluminous I-type rocks, except for some granitic rocks, which show a slight peraluminous trend.

Sr-Nd isotope systematics

Twelve samples from the main LHPC plutons were processed for Rb-Sr and Sm-Nd isotopic ratios and analytical results are compiled in Table 3. All samples show values with initial εNd and $^{87}Sr/^{86}Sr$ in a small range from +4.3 to +6.2 and 0.7033 to 0.7038, respectively (Figure 5b). All samples form a linear trend from the most primitive gabbroic rocks to the more evolved granitic rocks, which is more consistent with the MPC than the PVB rocks. Neodymium model ages (T_{DM}) of most samples range from 380 to 490 Ma, with the exception of the La Huerta gabbros, which have older model ages from 740 to 840 Ma (Table 3). These ages are older than the crystallization age but similar to those obtained in the MPC (300–500 Ma) by Schaaf *et al.* (2022).

Geochronology

U-Pb zircon geochronology

Zircon U-Pb geochronology by LA-ICP-MS in zircon crystals was performed in eight samples from the LHPC, prior to high-resolution cathodoluminescence (CL) imaging (Figure 6). Rough data can be consulted in Supplementary File 2. To facilitate the data visualization, weighted mean age diagrams are presented. The Wetherill Concordia diagrams for all samples are compiled in Supplementary File 3.

A monzogranite from the Cihuatlán pluton (MS 18a) was originally dated by Schaaf *et al.* (2022) in 80.57 ± 0.22 Ma (n = 33) and is shown here again (Figure 7a) because we additionally separated titanite crystals from this outcrop. Their analytical data are given in Supplementary File 4 and are plotted in a Tera-Wasserburg concordia diagram yielding an age of 75.94 ± 2.34 Ma based on 30 U-Pb determinations (Figure 7b), which is interpreted as a cooling age. Zircon grains from the Cuitzmala pluton (PVA19-22) yielded an age of 80.63 ± 0.45 Ma (n = 18) (Figure 7a). However, zircon grains from the chilled margin of the Cuitzmala pluton (PVA19-7) show a younger weighted mean age of 79.62 ± 0.35 Ma (n = 22, Figure 7a). Zircon grains from the El Chico pluton (PVA 19-11) show fine magmatic zoning and resorption bays (Figure 6). The latter is indicative of postmagmatic zircon alteration and likely responsible for the slightly older weighted mean age of 83.73 ± 0.35 Ma (n = 15) for this sample. Ages from the hybrid plutons were obtained from three lithologies. A sample (PVA20-10A) from the granitic component of the El Totole pluton yielded a weighted mean age of 76.05 ± 0.61 Ma (n = 16), which is similar to the age of the hybrid hornblende-gabbro (PVA19-9A) from the same pluton (75.56 ± 0.30 Ma, n = 30). A hybrid quartz-diorite from the Los Cimientos pluton (PVA19-24) shows low-luminescence zircon cores with fine oscillatory zoning (Figure 6). The weighted mean age of these zircon analyses yielded an age of 71.01 ± 0.33 Ma (n = 19), whereas those with high-luminescence rims yielded 68.37 ± 0.47 Ma (n = 13). Finally, detrital zircon grains were dated from a riverbed of a tributary to the Purification River (PVA 20-10B; Figure 1b) in order to constrain the presence of eroded magmatic rocks in the LHPC. Although the age of the main group corresponds to a peak *ca.* 78 Ma, some minor Cretaceous zircon grains (100–130 Ma) also occur (Figure 7c).

Rb-Sr biotite geochronology

Dating of biotites with Rb-Sr mineral- whole rock isochrons was performed in four samples (Table 3).

Biotite Rb-Sr ages for the Cuitzmala pluton were obtained from a monzogranite (PVA 19-15) and the chilled margin of the El Chico quartz-diorite (PVA 19-7) yielding 77.0 ± 0.6 Ma and 72.5 ± 0.5 Ma, respectively. Biotite rimmed by pyroxene from the Los Cimientos hybrid pluton (PVA 19-24) yielded an age of 73.1 ± 0.5 Ma. In the case of a hybrid hornblende gabbro from El Totole (PVA 19-9A), the obtained isochron age is 70.2 ± 0.5 Ma. These ages are interpreted as a stage of magmatic cooling around 400 °C (*e.g.*, Brown, 1971).

Ar-Ar geochronology in pyroxene from leucogabbro PVA 19-2

Clinopyroxene crystals from the La Huerta gabbros (leucogabbro PVA 19-2) were separated and analyzed by the $^{40}Ar/^{39}Ar$ method at Laboratorio Interinstitucional de Geocronología de Argón (LIGAr), Centro de Geociencias, UNAM-Campus Juriquilla. Analytical procedures are provided in Supplementary File 1 and raw data in Supplementary File 5. The age spectrum calculated using an initial atmospheric $^{40}Ar/^{36}Ar$ value of 295.5 did not yield an acceptable plateau (Supplementary File 5), whereas in the inverse isochron diagram, nine high-temperature gas fractions, corresponding to ~72 % of ^{39}Ar released, define an age of 77.64 ± 0.44 Ma (1σ; MSWD = 1.6) and a $^{40}Ar/^{36}Ar$ ratio of 306.1 ± 0.8 (1σ) for the trapped argon, which is indicative of excess ^{40}Ar (Figure 8). Using the trapped $^{40}Ar/^{36}Ar$ composition from the inverse isochron, a slightly more precise plateau age of 77.63 ± 0.30 Ma (1; MSWD = 0.89) was calculated for the same steps. The supra-atmospheric $^{40}Ar/^{36}Ar$ initial ratios in low-K minerals such as pyroxene have been related to the incorporation of fluids, melts, or minerals at the time of crystallization (*e.g.*, Kelley, 2002; Konrad *et al.*, 2019). In the analyzed sample, this seems to be supported by the increase in Ca/K ratios that yield older apparent ages in low-temperature steps and in intermediate to high-temperature steps of the age spectrum (Supplementary File 5). This age is also interpreted as a cooling age around 700–800 °C (Cassata *et al.*, 2011).

Trace element characteristics in zircons

The zircon trace-element concentration provides a geochemical proxy for cooling and fractional crystallization of the host magma. In this work, we combine zircon age, Th/U, Eu/Eu*, and Yb/Gd variations (Ferry and Watson, 2007; Fu *et al.*, 2008; Luo *et al.*, 2015; Schoene *et al.*, 2012; Kirkland *et al.*, 2015) to obtain petrochronological information recorded during zircon crystallization. Rough data can be consulted in Supplementary File 2. The Ti-in-zircon content relative to the zircon age does not show a linear tendency (Figure 9a), suggesting Ti fractionation in other phases during crystallization. However, by combining age and Ti-in-zircon content and thermometry with some trace element ratios it is possible to discriminate zircon groups with different petrogenetic information (Figure 9b–9d): (1) ~80 Ma rocks show narrow ranges of Th/U, Eu/Eu*, and Yb/Gd (0.2–0.8, 0.0–0.3, and 5–22, respectively) and a wide variation of Ti (5–35 ppm); (2) ~75 Ma rocks with higher values of Th/U and Eu/Eu* relative to the other age groups (0.7–1.8 and 0.0–0.3) and a Ti content between 0–20 ppm; and (3) ~70 Ma rocks with narrow ranges of Ti and Th/U (0–10 ppm and 0.2–0.7, respectively) and larger variations of Eu/Eu* and Yb/Gd (0.0–0.6 and 15–50, respectively). These values likely reflect different fractionation degrees of Ca-plagioclase, clinopyroxene, or hornblende during the early stages of magma crystallization (Schoene *et al.*, 2012; Luo *et al.*, 2015).

Thermobarometry

To estimate pressure and temperature (P-T) and other physical conditions such as oxidation state during the emplacement of LHPC rocks, several conventional barometers and thermometers were used in different mineral phases and assemblages. A summary of the main

Table 3. Rb-Sr and Sm-Nd isotopic compositions of LHPC whole rock and biotite samples. Methodological details can be consulted in Supplementary File 1. * Samples from Schaaf (1990) published in Schaaf *et al.* (2022). Biotite WR ages were calculated with the IsoplotR program (Vermeesch, 2018) using 1 SE errors. Ages are given with 1 sigma errors. 1 sd and 1 SE errors are given with the last digit(s).

Sample	Lithology	Petrographic classification	Pluton	$^{87}Rb/^{86}Sr$	$^{87}Sr/^{86}Sr$	1 sd*	1 SE(M)	n	$^{147}Sm/^{144}Nd$	$^{143}Nd/^{144}Nd$	1 sd*	1 SE(M)	n	εNd
PVA19-2	Gabbroic rocks	Leucogabbro	La Huerta gabbroic body	0.029	0.703540	32	4	56	0.181	0.512913	16	2	67	5.36
PVA19-3	Gabbroic rocks	Leucotroctolite	La Huerta gabbroic body	0.044	0.703378	29	4	56	0.156	0.512934	14	2	66	5.77
PVA19-7	Quartz-dioritic chilled margin	Hybrid quartz-diorite	Cuitzmala pluton	0.757	0.704392	33	4	56	0.130	0.512875	12	1	66	4.62
PVA19-9a	Quartz-dioritic to gabbroic hybrid rocks	Hybrid hornblende gabbro	El Totole pluton	0.201	0.703802	35	5	58	0.143	0.512894	12	1	65	4.99
PVA19-11	Quartz-dioritic chilled margins	Quartz-diorite	El Chico pluton	1.098	0.704890	33	4	59	0.130	0.512878	13	2	67	4.68
PVA19-13	Granitic to granodioritic rocks	Monzogranite	Cuitzmala pluton	1.357	0.705301	32	4	58	0.113	0.512813	13	2	70	3.41
PVA19-15	Granitic to granodioritic rocks	Monzogranite	Cuitzmala pluton	1.269	0.705150	29	4	57	0.116	0.512828	11	1	65	3.71
PVA19-17a	Gabbroic rocks	Leucogabbro	La Huerta gabbroic body	0.064	0.703636	31	4	58	0.159	0.512914	13	2	67	5.38
PVA19-18a	Gabbroic rocks	Leucotroctolite	La Huerta gabbroic body	0.060	0.703509	36	5	59	0.140	0.512904	13	2	68	5.19
PVA19-22	Granitic to granodioritic rocks	Monzogranite	Cuitzmala pluton	1.545	0.705378	35	5	58	0.106	0.512852	13	2	67	4.17
PVA19-24	Quartz-dioritic to gabbroic hybrid rocks	Hybrid quartz-diorite	Los Cimientos pluton	0.281	0.703977	38	5	58	0.149	0.512884	14	2	67	4.80
PVA19-25	Gabbroic rocks	Leucogabbro	La Huerta gabbroic body	0.147	0.703847	34	4	59	0.170	0.512882	13	2	67	4.76
Ms18a*	Granitic to granodioritic rocks	Granodiorite	Cihuatlán pluton	0.573	0.704115	39	5	60	0.110	0.512892	37	7	30	4.95
Ms19*	Granitic to granodioritic rocks	Granite	Cihuatlán pluton	1.329	0.704889	54	7	60	0.093	0.512861	48	6	60	3.01

Sample	Mineral	Pluton	$^{87}Rb/^{86}Sr$	$^{87}Sr/^{86}Sr$	1 sd*	1 SE(M)	n	-	-	-	-	-	-
PVA19-7	Quartz-dioritic chilled margins	Biotite	Cuitzmala pluton	60.22	0.764647	36	5	59	-	-	-	-	-	-
PVA19-9a	Quartz-dioritic to gabbroic hybrid rocks	Biotite	El Totole pluton	97.97	0.799701	34	4	58	-	-	-	-	-	-
PVA19-15	Granitic to granodioritic rocks	Biotite	Cuitzmala pluton	68.23	0.777210	34	4	58	-	-	-	-	-	-
PVA19-24	Quartz-dioritic to gabbroic hybrid rocks	Biotite	Los Cimientos pluton	26.13	0.730409	31	4	55	-	-	-	-	-	-

				Concentration (Isotope Dilution)				Nd model age (Ma)	Initial values (80 Ma)		
Sample	Lithology	Petrographic classification	Pluton	Rb (ppm)	Sr (ppm)	Sm (ppm)	Nd (ppm)		$^{87}Sr/^{86}Sr$	$^{143}Nd/^{144}Nd$	εNd
PVA19-2	Gabbroic rocks	Leucogabbro	La Huerta gabbroic body	5.73	569.99	1.87	6.26	841	0.703507	0.512818	5.53
PVA19-3	Gabbroic rocks	Leucotroctolite	La Huerta gabbroic body	7.60	497.23	2.60	10.11	413	0.703328	0.512853	6.20
PVA19-7	Quartz-dioritic chilled margin	Hybrid quartz-diorite	Cuitzmala pluton	99.94	381.70	5.49	25.45	396	0.703531	0.512807	5.30
PVA19-9a	Quartz-dioritic to gabbroic hybrid rocks	Hybrid hornblende gabbro	El Totole pluton	34.43	495.00	4.36	18.40	428	0.703574	0.512819	5.54
PVA19-11	Quartz-dioritic chilled margins	Quartz-diorite	El Chico pluton	125.79	331.47	6.84	31.85	389	0.703642	0.512810	5.36
PVA19-13	Granitic to granodioritic rocks	Monzogranite	Cuitzmala pluton	83.59	178.20	2.14	11.45	422	0.703758	0.512754	4.27
PVA19-15	Granitic to granodioritic rocks	Monzogranite	Cuitzmala pluton	86.44	197.10	2.38	12.37	413	0.703708	0.512767	4.53
PVA19-17a	Gabbroic rocks	Leucogabbro	La Huerta gabbroic body	11.36	515.90	2.97	11.30	494	0.703564	0.512831	5.77
PVA19-18a	Gabbroic rocks	Leucotroctolite	La Huerta gabbroic body	11.42	550.03	2.48	10.75	386	0.703441	0.512831	5.77
PVA19-22	Granitic to granodioritic rocks	Monzogranite	Cuitzmala pluton	91.49	171.35	2.53	14.37	341	0.703622	0.512796	5.10
PVA19-24	Quartz-dioritic to gabbroic hybrid rocks	Hybrid quartz-diorite	Los Cimientos pluton	44.59	459.61	5.26	21.33	490	0.703658	0.512806	5.29
PVA19-25	Gabbroic rocks	Leucogabbro	La Huerta gabbroic body	32.62	640.38	2.79	9.90	741	0.703680	0.512793	5.03
Ms18a*	Granitic to granodioritic rocks	Granodiorite	Cihuatlán pluton	66	334	2.7	14.7	296	0.703465	0.512834	5.83
Ms19*	Granitic to granodioritic rocks	Granite	Cihuatlán pluton	209	91	2.59	24.96	297	0.703340	0.512888	6.71

Sample	Mineral	Pluton	Rb (ppm)	Sr (ppm)	-	-	Rb-Sr WR-Bi age (Ma)	$^{87}Sr/^{86}Sri$	-	-
PVA19-7	Quartz-dioritic chilled margins	Biotite	Cuitzmala pluton	640.07	30.93			72.49±0.53	0.703625		
PVA19-9a	Quartz-dioritic to gabbroic hybrid rocks	Biotite	El Totole pluton	222.36	6.63			70.17±0.51	0.703605		
PVA19-15	Granitic to granodioritic rocks	Biotite	Cuitzmala pluton	435.38	18.59			76.98±0.56	0.703784		
PVA19-24	Quartz-dioritic to gabbroic hybrid rocks	Biotite	Los Cimientos pluton	305.22	33.88	-	-	73.15±0.53	0.703690	-	-

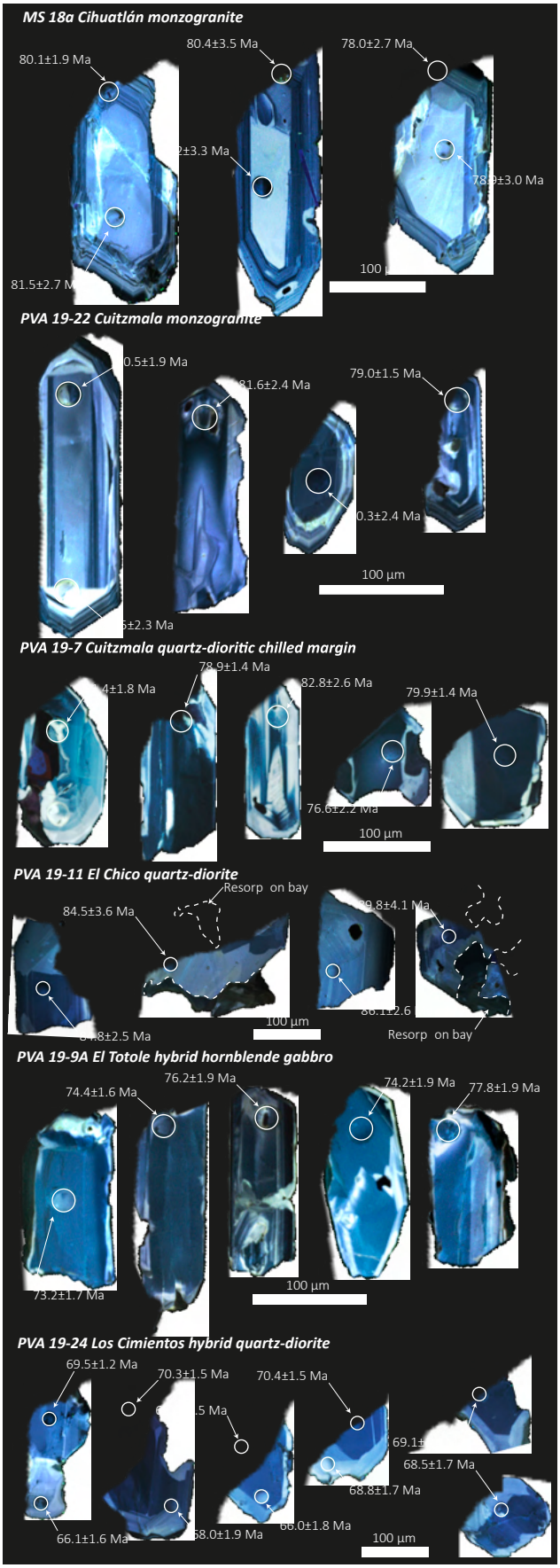

Figure 6. Cathodoluminescence images of representative zircon crystals used for LA-ICP-MS geochronology. Circles (of 25 µm diameter) indicate laser spot locations with their corresponding $^{206}Pb/^{238}U$ ages and 2σ errors (Supplementary File 2).

results is presented in Supplementary File 6. In the La Huerta gabbros, the pressure was determined from a leucotroctolite sample with an equilibrium assemblage of Ca-plagioclase, olivine, orthopyroxene, and clinopyroxene by employing the FACE barometer (Fumagalli *et al.*, 2017). The calculation yields 3.5 ± 0.3 kbar (SD = 0.1). Regarding granitic rocks (*sensu lato*), P-T conditions were estimated between 2.0 and 1.8 kbar using the Al-in-hornblende barometer (Mutch *et al.*, 2016) coupled with an amphibole-plagioclase thermometer (Holland and Blundy, 1994). The Cihuatlán, Cuitzmala, and El Chico plutons (~80 Ma) show a decreasing trend from ~750 °C and 2.0 kbar to ~500 °C and ~1.0 kbar (Figure 10a). On the other hand, P-T conditions from the Los Cimientos and El Totole hybrid plutons (~75–70 Ma) range from ~900 °C and ~1.5 kbar to ~700 °C and 2.5 kbar (Figure 10a). The chemical parameter X_{Mg} in amphibole shows similar variations relative to temperature, which is likely related to the oxidation state (Ridolfi *et al.*, 2010) (Figure 10b). The ~80 Ma plutons show an increasing oxidation trend (-15.7 to -12.1) with decreasing temperature. On the other hand, ~75 to 70 Ma hybrid plutons show a decreasing trend (-13.7 to -12.6) with decreasing temperatures (Figure 10b).

Ti-in-biotite thermometry was performed according to Henry (2005). Most of the samples show relatively low temperatures between ~520° and 660 °C, whereas high-Mg biotites from leucotroctolites and hybrid chilled-margins show higher temperatures from ~680° to 710 °C (Figure 10b).

The aforementioned temperatures represent relative equilibria states during the crystallization of the plutonic bodies. To obtain a better estimation of the crystallization temperature, Ti-in-zircon thermometry was performed for all dated plutons (Supplementary File 6) considering $a_{SiO_2} = 1.0$ and $a_{TiO_2} = 0.7$ (Claiborne *et al.*, 2010; Ferry and Watson, 2007). Crystallization temperatures of ~80 Ma granitic zircons range from ~700° to 850 °C (mean temperatures). The highest temperatures correspond to quartz-diorites from the El Chico pluton (790°C, SD = 40 and 855 °C, SD = 34), whereas the lowest temperatures belong to the Cihuatlán and Cuitzmala monzogranites (771°C, SD = 30 and 715 °C, SD = 59, respectively). Ti-in-zircon temperatures from the El Totole hybrid pluton are similar in both hybrid and non-hybrid rocks with mean values of 752 °C (SD = 51) and 761 °C (SD = 63) respectively, and record a higher mean crystallization temperature than the Los Cimientos hybrid quartz-diorite (670 °C, SD = 18; Figure 9a).

DISCUSSION

Petrogenesis and lithological diversity of the LHPC

The great compositional diversity of plutonic rocks of the LHPC requires the integration of many hypotheses concerning their petrogenesis and the coexistence of gabbroic and granitic rocks in continental subduction zones.

High K_2O content of hybrid rocks is explained by mingling structures and enrichment of K feldspar crystals mechanically infiltrated from granitic melts (Figure 3). The alkaline trend in some gabbroic rocks can be related to peritectic Mg-biotite in the troctolites and secondary alteration phases in the leucogabbros. Trace element geochemistry reveals that LHPC granitic to gabbroic rocks originated from subduction-related continental arc magmatism according to the Th-Ta-Yb discrimination diagrams (Figure 5c). The petrogenesis of the

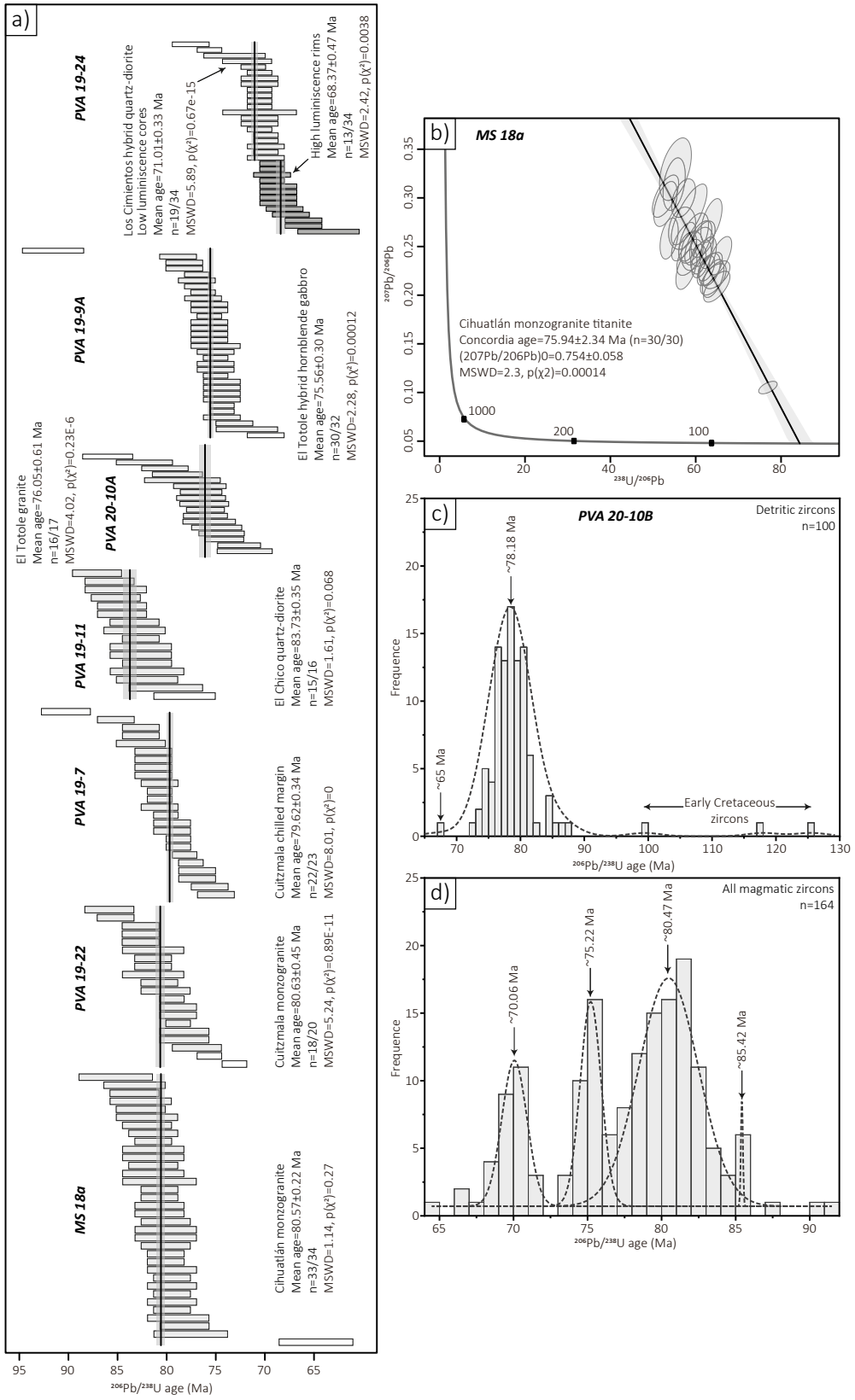

Figure 7. U-Pb geochronology of the LHPC rocks. All plots, ages, and errors were performed with the IsoplotR software (Vermeesch, 2018) a) $^{206}Pb/^{238}U$ weighted mean ages for zircon crystals of granitic rocks *(sensu lato)* and hybrid rocks. Each bar represents an individual analysis and their vertical size are 2σ errors, white bars are data not considered in the mean age. b) Tera-Wasserburg diagram with LA-ICP-MS U-Pb titanite ages from the Cihuatlán granite. Each ellipse represents an individual analysis and their 2σ error. c) KDE diagram for the detrital zircons of riverbed sample PVA 20-10b. d) KDE plot for all magmatic zircon data, which suggests at least three main magmatic events. The peaks were calculated by Gauss deconvolution.

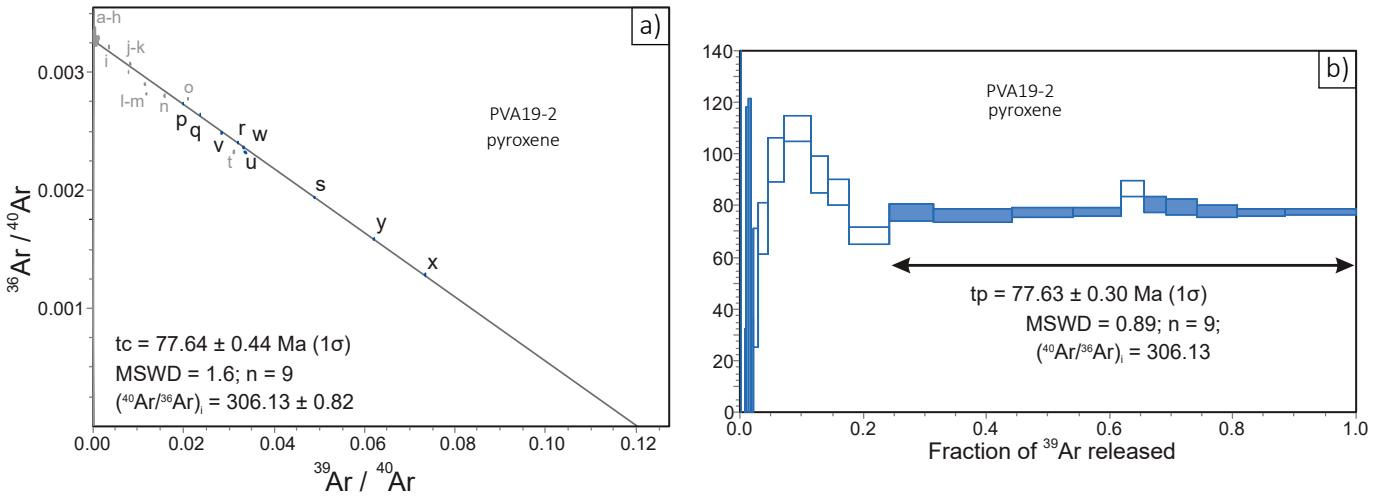

Figure 8. a) $^{40}Ar/^{39}Ar$ inverse isochron diagram and b) step-heating age spectrum for analysed clinopyroxene crystals from leucogabbro PVA 19-2. The graphs include the correlation age (tc), the initial $^{40}Ar/^{36}Ar$ ratio, the plateau age (tp), % of released ^{39}Ar, and the number of steps (n) used in the age calculation. MSWD: mean squared weighted deviation.

mafic rocks appears to be related to a mantellic source hydrated during a subduction process (Figures 5c–5d), which agrees with the trend of the MPC mafic rocks. On the other hand, granitic to quartz-dioritic hybrid rocks show high-Th/Yb ratios relative to the mafic samples (Figures 5c–5d) which support an origin related to mixing with crustal-derived melts. The La/Yb and Sm/Yb ratios suggest that the origin of the gabbros is related to a low-grade partial melting of garnet peridotites (Figure 5e) during the slab dehydration in a subduction process. A good correlation with the MPC gabbroic rocks is also evident in Figure 5d.

The La Huerta gabbros are dominated by leucogabbros intruded by leucotroctolitic dikes, both with textural evidence of cummulitic plagioclase produced by fractional crystallization (Figure 3). The case of leucotroctolite petrogenesis in ophiolitic assemblages has been attributed to reactions between MORB-type magmas and mantellic rocks (O'Driscoll *et al.*, 2010; Renna and Tribuzio, 2011). In the case of continental arc magmatism, the reaction between primary mafic magmas and the sublithospheric mantle can generate troctolitic magmas (Buchko *et al.*, 2012). On the other hand, olivine compositions from La Huerta leucotroctolites ($Fo_{57\text{-}56}Fa_{42\text{-}43}$) are not compatible with typical olivine of ophiolitic troctolites ($Fo_{80}Fa_{20}$) (O´Driscoll *et al.,* 2010; Renna and Tribuzio, 2011). Instead, they are compatible with H_2O subsaturation conditions during differentiation of gabbroic magmas (Koszowska *et al.*, 2007). Initial Sr-Nd isotope ratios of LHPC gabbroic rocks ($\varepsilon Nd_i = +5.0$ to $+6.2$, $^{87}Sr/^{86}Sr_i = 0.7033\text{-}0.7037$) as well as Rb-Sr isotope ratios from troctolitic Mg-biotites (PVA 19-3: Rb/Sr = 2.3, $^{87}Rb/^{86}Sr = 6.77$ and $^{87}Sr/^{86}Sr = 0.711562$, Table 3) support the mantle affinity of the La Huerta gabbros (Grégoire *et al.*, 2002; Efimov *et al.*, 2012; Fritschle *et al.*, 2013).

Petrogenesis of granitic rocks is related to partial melting of lower continental crust, according to their $(La/Yb)_N$ and Sr/Y ratios (Figure 5f) and similar to the granitic rocks from the PVB, suggesting an origin related to the 20–25 % of partial melting of garnet peridotite promoted by slab dehydration (Figures 5c–5e). Following the hypothesis that calc-alkaline granitic melts in continental arc settings are derived from andesites related to the partial melting of a metasomatized mantle wedge (*e.g.*, Straub *et al.*, 2014; Gómez-Tuena *et al.*, 2018; Castro, 2019; Triantafyllou *et al.*, 2020), the LHPC granitic rocks can represent a case of low crustal assimilation during ascent and emplacement, as evidenced by primitive Sr-Nd isotope ratios ($\varepsilon Nd_i = +4.2$ to $+5.3$, $^{87}Sr/^{86}Sr_i = 0.7035\text{-}0.7038$, Figure 5b) and the absence of inherited zircon cores (Figure 6). Variations in zircon trace element content of granitic rocks are likely a reflection of Ca-plagioclase, amphibole, or pyroxene fractionation during crystallization (Figure 9), which is consistent with the presence of clinopyroxene inclusions in plagioclase crystals (Figure 3e). Although this feature is negligible in rocks from chilled margins (*e.g.*, PVA 19-22), it is evident that ~80 to 70 Ma granitic rocks have a similar petrogenesis and evidence of fractional crystallization or the formation of a residue during the segregation of primary granitic magmas. These two processes, partial melting of the lower crust and fractional crystallization, can be responsible for the generation of the granitoids observed in LHPC, as has been proposed by many authors (*e.g.* Moyen *et al.*, 2021).

The intermediate hybrid plutonic rocks, which result from the mixing between granitic and gabbroic melts, still preserve primary hornblende gabbros at different scales. The petrogenesis of the hornblende gabbros is distinctive from the other LHPC gabbroic rocks because they are more common in continental arc settings (*e.g.*, Xie *et al.*, 2019). Ca-plagioclase and hornblende-saturated magmas require partial melting of a metasomatized and H_2O oversaturated mantellic source (Sisson and Grove, 1993; Prouteau *et al.*, 2001; Xie *et al.*, 2019), which can occur in an overhydrated mantle wedge due to slab dehydration.

Age and spatial relationships of the LHPC

The age of the plutonic rocks from LHPC was determined by U-Pb, $^{40}Ar/^{39}Ar$, and Rb-Sr geochronometers, which allowed us to discriminate between four plutonic stages. Fieldwork strongly suggests that the oldest LHPC magmatic event corresponds to the La Huerta gabbros. However, this could not be dated directly due to the absence of zircon in SiO_2 subsaturated melts (*e.g.*, Schaltegger and Davies, 2017). Instead, a leucotroctolite was dated with $^{40}Ar/^{39}Ar$ in clinopyroxene, yielding an age of 77.97 ± 0.99 Ma (Figure 8), interpreted as a cooling age corresponding to a closure temperature of 700–800 °C (Cassata *et al.*, 2011). However, due to the cummulitic origin of pyroxenes in this rock, this age probably corresponds to a mean cooling-age of the analyzed crystals.

Granitic rocks represent the most voluminous magmatism in the LHPC. They contain zircon U-Pb ages ranging from 79.6 to 83.7 Ma (Figure 7) considered to represent the emplacement and crystallization of these plutons. These U-Pb ages are correlative with the main granitic to granodioritic event in the PVB (80-85 Ma; Schaaf *et al.*, 2020). In the case of the Cihuatlán pluton (a border pluton with the Manzanillo Plutonic Complex) an additional U-Pb age of 75.9 Ma was determined

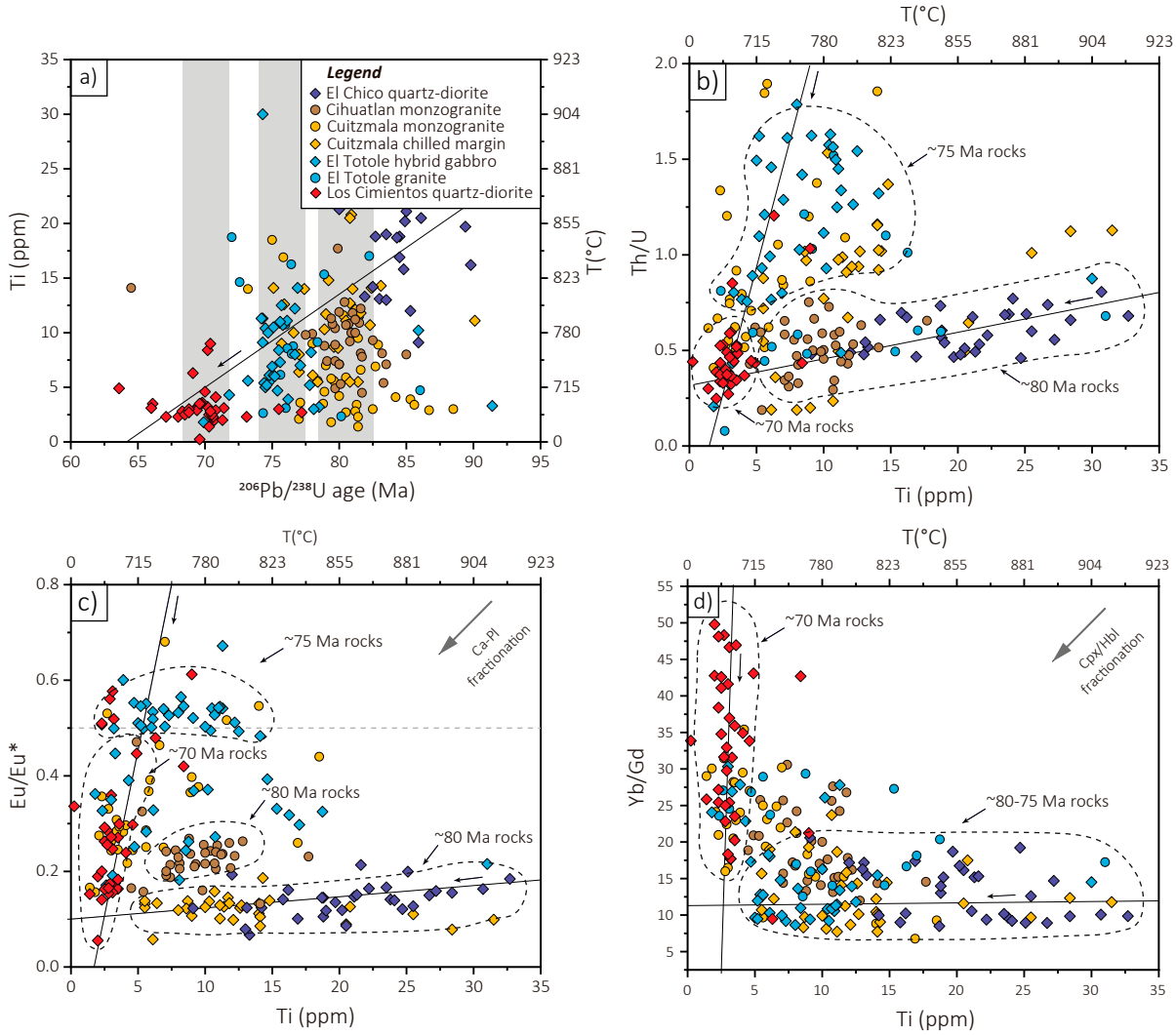

Figure 9. Zircon trace elements vs. time determined by LA-ICP-MS. Symbols are the same as in Figure 5. Arrows indicate geochemical trends with time and areas with dashed borders correspond to three main magmatic events described in the geochronology section. a) Ti content and temperature *vs.* age diagram. Ti-in-zircon temperature was determined according to Ferry and Watson (2007), using a_{SiO_2}=1.0, and a_{TiO_2}=0.7 (Claiborne *et al.*, 2010). The rest of the geochemical proxies are also plotted with respect to Ti content and crystallization temperature: Th/U *vs.* Ti (b), Eu/Eu* *vs.* Ti (c), and Yb/Gd *vs.* Ti (d).

from magmatic titanite (Figure 7b) interpreted as a cooling age between 550–650 °C (Corfu, 1988; Frost *et al.*, 2001). In this pluton, younger biotite – whole rock Rb-Sr ages of 69.5 ± 1.4 Ma and 64.7 ± 1.3 Ma (1 sigma errors) were reported previously by Schaaf *et al.* (2022) in samples MS18a and MS19, respectively. These are interpreted as reflecting isotopic resetting triggered by the neighboring MPC magmatic event.

Interpretation of geochronological data for hybrid plutons requires a more careful analysis. In the case of El Totole pluton, hornblende gabbros and granites show similar zircon U-Pb ages (75.5 and 76.0 Ma, respectively; Figure 7). However, this is inconsistent with the observed field relationships where granitic rocks are intruding and mixing with the hornblende gabbros. On the other hand, amphibole-plagioclase thermometry in the hornblende gabbro (851 ± 40 °C, S.D. = 16) shows a higher temperature with respect to the Ti-in-zircon saturation temperature (584 ± 12 °C, S.D. = 17). Based on the thermometric evidence and that zircon precipitation is unlikely in Si-poor melts, zircon crystals from the El Totole hornblende gabbro possibly crystallized after the amphibole-plagioclase assemblage. Therefore, the U-Pb age of 75.56 ± 0.30 Ma rather corresponds to the hybridization process. In fact, biotites in the hybrid gabbros are texturally characterized by replacement with hornblende. The corresponding Rb-Sr biotite-whole rock age of 70.17 ± 0.02 Ma (Table 3) can be related to the final consolidation stage.

Zircon grains from the quartz-diorite member of Los Cimientos hybrid pluton, show core-mantle textures with brighter luminescence at the rims. Zircon cores yield a weighted mean age of 71 Ma, whereas rims yield 68.3 Ma. (PVA 19-24; Figure 7). Based on zircon trace element concentrations these ages cannot be related to distinctive magmatic events and probably represent a two-stage protracted crystallization process. This rock exhibits biotite surrounding pyroxene (Figure 3i) indicating a solvation process during an early hybridization stage at ~73.15 Ma based on the biotite Rb-Sr isochron age (Table 3).

Crystallization ages between 70–75 Ma have been poorly documented in the PVB (Schaaf *et al.*, 2020). One exception is the Tio Cleto dioritic pluton of the northern PVB with ages ranging between 60-72 Ma (Valencia *et al.*, 2013). In the case of the MPC, the La Laguna pluton yielded a U-Pb zircon age of 73 ± 1 Ma (Panseri, 2007). Other ages documented in the LHPC correspond to hornblende and biotite K-Ar cooling ages between 66 and 70 Ma (Gastil *et al.*, 1976; Solé *et al.*, 2007; Figure 1b) which correlate with the 70-75 Ma magmatism and

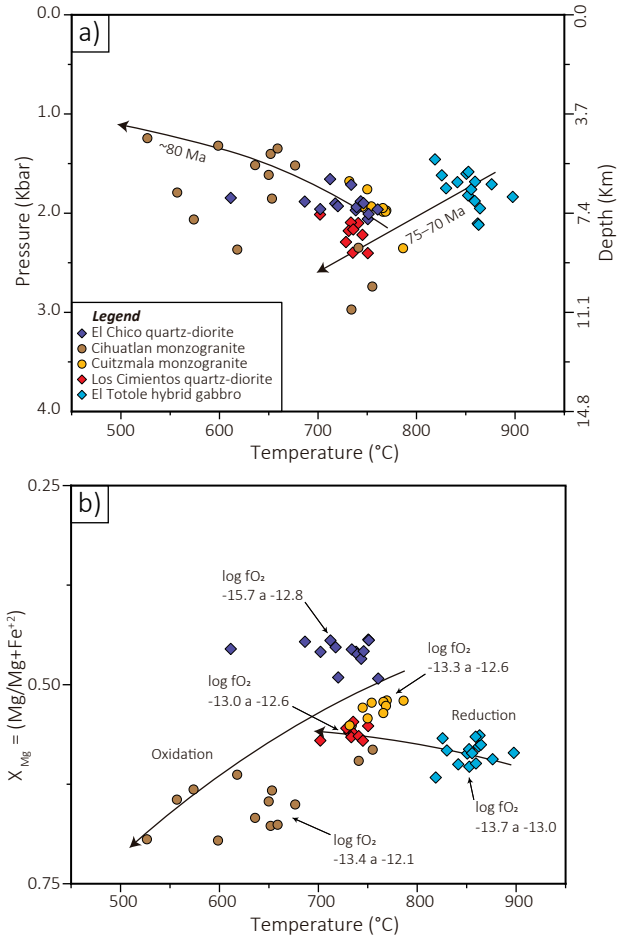

Figure 10. LHPC thermobarometry. a) Temperature *vs.* pressure *vs.* depth diagram. The temperature was estimated by Al-in-hornblende saturation (Mutch *et al*., 2016), and temperature by plagioclase-amphibole equilibria (Holland and Blundy, 1996). Arrows indicate trends with the same lithology and age. b) Temperature *vs.* X_{Mg} diagram with calculated QFM buffer oxygen fugacity (fO_2) for amphibole at each lithology. Oximetry was estimated after Ridolfi *et al.* (2010). Representative microchemical compositions are shown in Table 1 and a summary of thermobarometric determinations is given in Supplementary File 6.

hybridization event documented in this work. Finally, zircon grains older than 85 Ma in the analyzed samples, reveal the presence of early stages of zircon crystallization in the magma.

A Kernel Density Estimation (KDE) diagram of all data from magmatic zircons (n = 164) displays at least three magmatic episodes registered in the plutonic rocks of LHPC (Figures 7a and 7d): (1) a ~84–79 Ma event which corresponds to granitic to quartz-dioritic magmatism (*e.g.*, PVA 19-11, MS 18a, PVA 19-22), (2) 75-76 Ma peaks of hybrid and non-hybrid granitic to gabbroic rocks of El Totole (PVA 19-7, PVA 19-9A) and (3) 71–68 Ma hybrid quartz diorites from Los Cimientos (PVA 19-24).

Emplacement and magmatic evolution of the LHPC

According to petrographic observations, thermobarometric estimations, as well as geochemical and geochronological data, a four-stage magmatic model is proposed in this study (Figure 11a). The physical emplacement conditions of the LHPC intrusives were constrained by conventional thermobarometry. The interpretation of the thermobarometric techniques used in this work depends on the mineral or paragenesis analyzed. In this context, the Al-in-hornblende and FACE (Ca-plagioclase, olivine, orthopyroxene and clinopyroxene) barometers, as well as the Ti-in-zircon thermometer are considered markers for the physical conditions of the pluton emplacement, whereas other thermometers such as Ti-in-biotite or amphibole-plagioclase work as tracers for the post-magmatic thermal history of the intrusives.

Emplacement conditions of the La Huerta gabbros were constrained in the leucotroctolite dikes with the FACE geobarometer (Fumagalli *et al*., 2017) yielding pressure conditions between 3.2 and 3.6 kbar, whereas the temperature was estimated by the two pyroxene geothermometer of Putirka (2008), yielding >1000 °C. The results suggest *ca.* 12 km depth (middle to upper crust) for the emplacement of the leucotroctolite dikes. It is inferred that the host leucogabbros were intruded prior to the intrusion of the leucotroctolite dikes at >84 Ma within similar pressure conditions. Subsequently, the La Huerta gabbros were intruded at subsolidus conditions by the Cuitzmala granitic pluton.

According to the Al-in-hornblende barometer and amphibole-plagioclase thermometer, the granitoids were emplaced between 1.7 to 2.4 kbar (6 to 7 km depth of the upper crust) at 610 to 910 °C for the Cuitzmala and El Chico plutons and at 0.7 to 3.5 kbar (3.5 to 11 km) and 700 to 850 °C in the case of the Cihuatlán pluton. The thermobarometric data indicate that the gabbroic rocks were uplifted to shallower levels (reaching 6–7 km depth) prior to the intrusions of the acid-intermediate rocks.

The borders of the granitic plutons show clinopyroxene-rich quartz-dioritic compositions likely related to the mixing processes with the host gabbroic rocks. This is supported by the presence of Ca-rich plagioclase rims and the development of mafic phases such as Mg-biotite, clinopyroxene, and orthopyroxene. Mg-biotites in the Los Cimientos hybrid pluton show Ti-saturation temperatures of 690–710 °C, which are similar to the observed values in the Mg-biotites from La Huerta gabbroic rocks (690–700 °C).

The mafic microgranular enclaves (MMEs) contained in the granitic plutons have mineralogical and textural similarities with the quartz-dioritic rocks at the margins, which are probably related to a solidification edge/front (Holness *et al*., 2019). The diversity of morphologies and size of the MMEs, suggests that they are early crystallized fragments remobilized from the margins and reworked by convection currents. At the margins of some plutons, some enclaves may have reacted with the remaining magma developing reactions margins with the host and developing disequilibrium textures such as anti-rapakivi crystals and partial replacement of hornblende around pyroxene.

The 75–70 Ma magmatic event is characterized by mingling of hornblende gabbros and monzogranites between 1.5 and 2.4 kbar and 650 to 850°C in the upper crust. In the El Totole hybrid pluton, the mafic component is characterized by >75 Ma hornblende gabbros which were disrupted and dismembered by granitic intrusions of similar ages (75–76 Ma). In the Los Cimientos pluton, the mafic portion is preserved as enclaves hosted by hybrid quartz-diorite, whose ages evidence three crystallization stages from 73 to 68 Ma (based on biotite Rb-Sr and zircon U-Pb ages). Other hornblende gabbros occur as ovoid enclaves in the *ca.* 80 Ma Cihuatlán pluton, suggesting a moderate to high temperatures of the granitic intrusion at the time of enclave subtraction.

Tectonic implications and magmatic model of southwestern Mexico during the Cretaceous-Paleogene

Based on the analytical data documented in this work, it is interpreted that the LHPC formed through three continuous magmatic pulses. The petrogenesis of these pulses occurred in a continental subduction setting, previously proposed by many authors (*e.g.*, Valencia

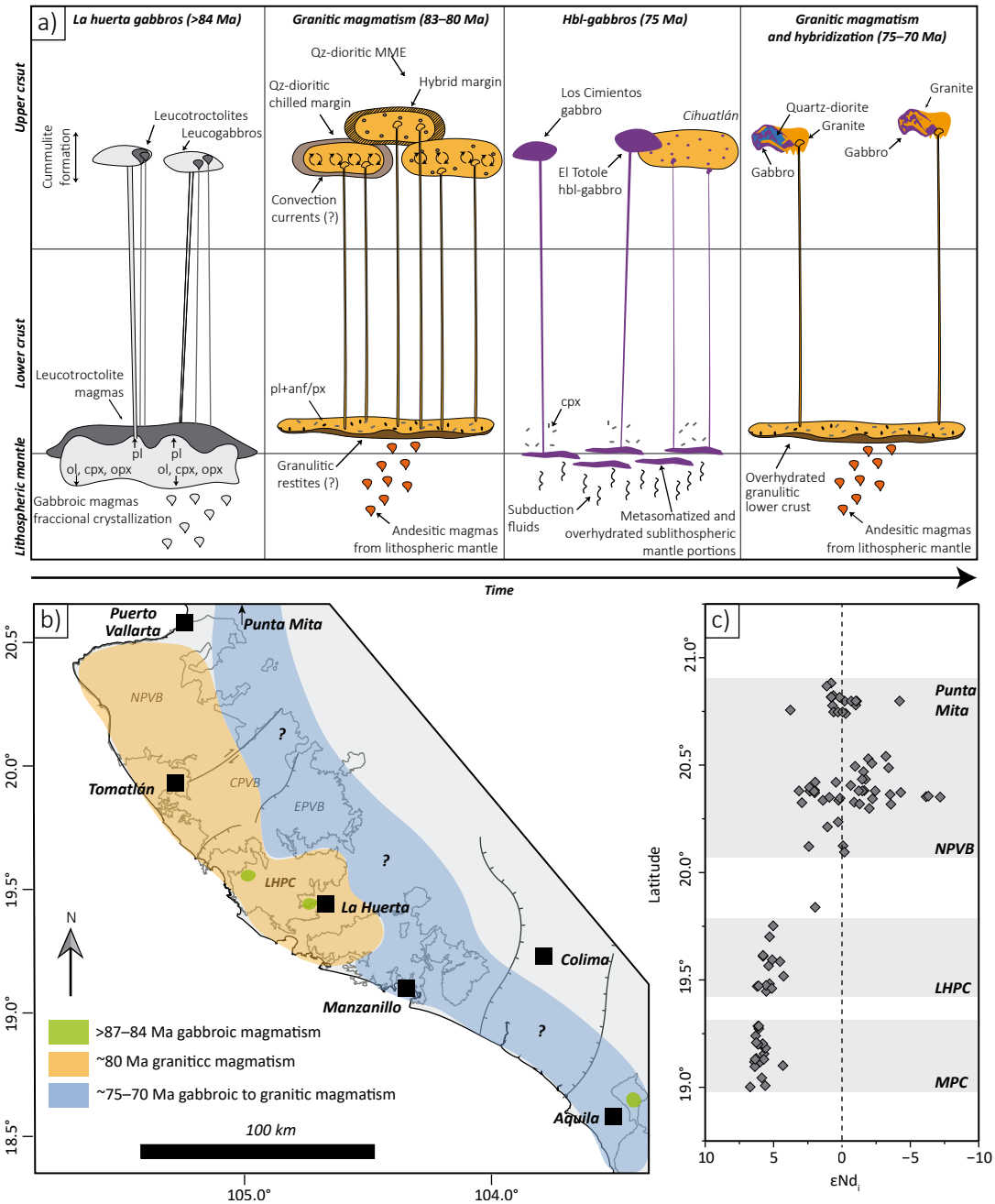

Figure 11. a) Magmatic emplacement model of the LHPC bodies and distribution along the W Mexican Pacific margin (b) of the main magmatic events recognized in the area. c) Latitude vs. initial εNd of the plutonic rocks exposed along de western Pacific Margin from this work and compiled from Schaaf *et al.* (2020; 2022) and Vite Sánchez (2019).

et al., 2013; Morán-Zenteno *et al.*, 2018; Schaaf *et al.*, 2020). Despite the inaccurate age estimations, the cummulitic gabbroic activity (>84 Ma) in the LHPC is interpreted as the first magmatic stage, resulting from partial melting of a metasomatized garnet-bearing peridotite (Figure 11a). The second LHPC magmatic event corresponds to the ~80 Ma granites, which is very voluminous and dominant in the area of the Jalisco Bock (Figure 11). Finally, the origin of the 70–75 Ma hybrid granitic-gabbroic rocks can be related to an inland arc migration (in the eastern region of the PVB) and partial melting of an overhydrated mantle and lower crust (Figure 11a). The eastward arc migration across the Jalisco Block was proposed by Valencia *et al.* (2013) to explain the presence of 72–60 Ma tonalitic to dioritic rocks in the north-eastern region of the NPVB and their correlation with the MPC. Therefore, the LHPC can be considered as the south-eastern limit of the PVB and the transitional bond with the western part of the MPC.

The extent of the magmatic events recorded in LHPC (~80 Ma and 75–70 Ma) can be traced to the northern part of the PVB and to the MPC, as shown in figure 11b. Notably, the gabbroic-troctolitic outcrops are restricted to the LHPC area (Figure 11b) with outcrops of similar age and lithology as in the Aquila Batholith (~83 Ma; Gómez Rivera, 2019). The ~80 Ma granitic event widely extends along the coast of the Jalisco block from the NPVB to Cihuatlán, whereas the 75–70 Ma magmatic event only occurred in the NPVB east of the city of Puerto Vallarta (Figure 11b). This pattern is also observed in the LHPC,

where 75–70 Ma hybrid plutons present the eastern inland position with respect to the granitic plutons and correlate with the La Laguna pluton in the MPC (Schaaf *et al*., 2022).

Despite the geochemical and geochronological similarities between the NPVB and LHPC, there is an important difference concerning emplacement depths and Sr-Nd isotopic ratios. In the NPVB, emplacement depths are between 5.9–3.1 kbar with $^{87}Sr/^{86}Sr$ and εNd between 0.7126 and 0.7010 and +2.4 to -7.2, respectively, which contrasts with the shallower and more primitive values for the LHPC (Figure 11c). This difference can be attributed to a thick crust in the northern Jalisco Block, which allowed the input of crustal material during the formation of these magmas and their emplacement into the middle crust. This trend (Figure 11c) is continuous from the NW to SE and characterizes the LHPC as an independent part of the PVB, with a thin crust where plutonism had a shallower emplacement depth and minor to negligible participation of isotopically evolved crustal material.

CONCLUSIONS

The La Huerta Plutonic Complex (LHPC) is composed of crustal epizonal intrusions (3.5 to 1.8 kbar) that were amalgamated between >84 Ma and 70 Ma. Cummulitic gabbroic rocks were emplaced at >84 Ma at ~3.5 kbar in the crust, which was intruded nearly simultaneously by a voluminous granitic event. The last magmatic episode registered in the area corresponds to shallow (2.0 kbar) mingled gabbroic to granitic intrusions between ~75 Ma to 70 Ma. The extent of these magmatic events has been recognized in the Puerto Vallarta Batholith (PVB) as well as in the Manzanillo Plutonic Complex (MPC).

Regionally, the LHPC is located between the two aforementioned batholiths and shares with both some petrological, geochemical, and geochronological features. The LHPC magmatic development can be considered as a transition between a ~80 Ma granitic-dominated magmatism and ~75 Ma to 70 Ma gabbroic to granitic magmatic events. The presence of scarce cummulitic gabbroic rocks represents the oldest magmatic event in the area, but their occurrence and extension along the Mexican Cordillera remains relatively restricted and unclear.

On the other hand, Sr-Nd isotopic and thermobarometric data show notable differences between the northern PVB intrusive rocks (initial εNd between +2.4 to -7.1 at 5.9 to 3.1 kbar) and those of the southern PVB (initial εNd between +4.2 to +6.2 at 3.5 to 1.8 kbar). These differences are interpreted as the result of different amounts of crustal contamination due to different thicknesses of the crust.

ACKNOWLEDGMENTS

This research was funded by Programa de Apoyo a Proyectos de Investigación e Innovación Tecnológica (PAPIIT) IN 115220, 109517 and IN 112314. We thank Rufino Lozano, Patricia Girón, and Santiago Avilés (Laboratorio Nacional de Geoquímica y Mineralogía, Instituto de Geología, UNAM) for XRF analyses, to Luigi Solari, Carlos Ortega-Obregón and Ofelia Pérez (Laboratorio de Estudios Isotópicos, Centro de Geociencias, UNAM) for LA-ICP-MS U-Pb isotopic age determinations in zircons, and ICP-MS trace element analyses, to Carlos Linares (Laboratorio Universitario de Petrología, Instituto de Geofísica, UNAM) for EPMA determinations, to Jazmín Díaz and Oscar Talavera (Laboratorio de Microscopía Electrónica y Microanálisis, Universidad Autónoma de Guerrero) for zircón CL images acquisition. Finally, we thank Teresa Orozco Esquivel and Gabriela Hernández Quevedo (Laboratorio Interinstitucional de Geocronología de Argón (LIGAr), Centro de Geociencias, UNAM) for Ar-Ar age determinations in pyroxene and Adriana Moreno Arredondo (LIGAr) for sample preparation. The LIGAr argon geochronology lab was supported by CONACYT infrastructure grants 224667 and 316372. Reviews by Guillermo Espejo and Juan Alonso Ramírez Fernández helped to improve the manuscript substantially.

SUPPLEMENTARY MATERIAL

The Supplementary Files 1 to 6 can be downloaded at the webpage of this journal <www.rmcg.unam.mx> in the abstract's preview page of this paper.

REFERENCES

Brown, E.H., 1971, Phase relations of biotite and stilpnomelane in the greenschist facies: Contributions to Mineralogy and Petrology, 31, 275-299.

Buchko, I.V., Sorokin, A.A., Ponomarchuk, V.A., Izokh, A.E., 2012, Geochemical features and geodynamic setting of formation of the Lukinda dunite–troctolite–gabbro massif (southeastern framing of the Siberian Platform): Russian Geology and Geophysics, 53(7), 636-648, https://doi.org/10.1016/j.rgg.2012.05.002.

Campa, M.F., Coney, P.J., 1983, Tectono-stratigraphic terranes and mineral resource distributions in Mexico: Canadian Journal of Earth Sciences, 20(6), 1040-1051, https://doi.org/10.1139/e83-094.

Cassata, W.S., Renne, P.R., Shuster, D.L., 2011, Argon diffusion in pyroxenes: Implications for thermochronometry and mantle degassing: Earth and Planetary Science Letters, 304(3-4), 407-416.

Castro, A., 2019, The dual origin of I-type granites: the contribution from experiments: Geological Society Special Publication, 491(1), 101-145, https://doi.org/10.1144/sp491-2018-110.

Centeno-García, E., Guerrero-Suastegui, M., Talavera-Mendoza, O., 2008, The Guerrero Composite Terrane of western Mexico: Collision and subsequent rifting in a supra-subduction zone: Geological Society of America Special Paper 436, Formation and Applications of the Sedimentary Record in Arc Collision Zones, 279-308.

Centeno-García, E., Busby, C., Busby, M, Gehrels G., 2011, Evolution of the Guerrero composite terrane along the Mexican margin, from extensional fringing arc to contractional continental arc: Geological Society of America Bulletin, 123, 1776-1797.

Claiborne, L.L., Miller, C.F., Wooden, J.L., 2010, Trace element composition of igneous zircon: a thermal and compositional record of the accumulation and evolution of a large silicic batholith, Spirit Mountain, Nevada: Contributions to Mineralogy and Petrology, 160(4), 511-531, https://doi.org/10.1007/s00410-010-0491-5.

Corfu, F., 1988, Differential response of U-Pb systems in coexisting accessory minerals, Winnipeg River Subprovince, Canadian Shield: implications for Archean crustal growth and stabilization: Contributions to Mineralogy and Petrology, 98(3), 312-325, https://doi.org/10.1007/bf00375182.

Efimov, A.A., Ronkin, Y.L., Malich, K.N., Lepikhina, G.A., 2012, New Sm-Nd and Rb-Sr (ID-TIMS) isotope data for apatite-phlogopite clinopyroxenites from the dunite "Core" of the Konder Massif, Aldan Shield, Yakutia: Doklady Earth Sciences, 445(2), 956-961, https://doi.org/10.1134/s1028334x12080120.

Ferry, J.M., Watson, E.B., 2007, New thermodynamic models and revised calibrations for the Ti-in-zircon and Zr-in-rutile thermometers: Contributions to Mineralogy and Petrology, 154(4), 429-437, https://doi.org/10.1007/s00410-007-0201-0.

Foster, M.D, 1960, Interpretation of the composition of trioctahedral micas: U.S. Geological Survey Professional Paper, 354-B, 1-49.

Fritschle, T., Prelević, D., Foley, S. F., Jacob, D. E., 2013, Petrological characterization of the mantle source of Mediterranean lamprolites: Indications from major and trace elements of phlogopite: Chemical Geology, 353, 267-279, https://doi.org/10.1016/j.chemgeo.2012.09.006.

Frost, B.R., Frost, C.D., 2008, A geochemical classification for feldspathic

igneous rocks: Journal of Petrology, 49(11), 1955-1969, https://doi.org/10.1093/petrology/egn054.

Frost, B.R. Chamberlain, K.R., Schumacher, J.C., 2001, Sphene (titanite): phase relations and role as a geochronometer: Chemical Geology, 172(1-2), 131-148, https://doi.org/10.1016/s0009-2541(00)00240-0.

Fu, B., Page, F.Z., Cavosie, A.J., Fournelle, J., Kita, N.T., Lackey, J.S., Valley, J.W., 2008, Ti-in-zircon thermometry: applications and limitations: Contributions to Mineralogy and Petrology, 156(2), 197-215.

Fumagalli, P., Borghini, G., Rampone, E., Poli, S., 2017, Experimental calibration of Forsterite–Anorthite–Ca-Tschermak–Enstatite (FACE) geobarometer for mantle peridotites: Contributions to Mineralogy and Petrology, 172(6), https://doi.org/10.1007/s00410-017-1352-2.

Gastil, G., Krummenacher, D., Douppont, J., Bushee, J., Barthelmy, D., 1976, La zona batolítica del sur de California y el occidente de México: Boletín de La Sociedad Geológica Mexicana, 37(2), 84-90, https://doi.org/10.18268/bsgm1976v37n2a3.

Gómez Rivera, F.J., 2019, Análisis petrológico e isotópico del Complejo Batolítico Aquila, suroccidente de México: Morelia, Mich. Mexico, Universidad Michoacana de San Nicolás de Hidalgo, M. Sc. Thesis, 103 pp.

Gómez-Tuena, A., Mori, L., Straub, S.M., 2018, Geochemical and petrological insights into the tectonic origin of the Transmexican Volcanic Belt: Earth-Science Reviews, 183, 153-181, https://doi.org/10.1016/j.earscirev.2016.12.006.

Grégoire, M., Bell, D., Le Roex, A., 2002, Trace element geochemistry of phlogopite-rich mafic mantle xenoliths: their classification and their relationship to phlogopite-bearing peridotites and kimberlites revisited: Contributions to Mineralogy and Petrology, 142(5), 603-625, https://doi.org/10.1007/s00410-001-0315-8.

Gutiérrez-Aguilar, F., Hernández-Uribe, D., Vite-Sánchez, O., Schaaf, P., Arrieta-García, G.F., Solís-Pichardo, G., Hernández-Treviño, T., 2021a, New insights into the petrogenesis of the Puerto Vallarta Batholith, Mexico: Evidence from petrology, zircon petrochronology, and phase equilibrium modelling: Journal of South American Earth Sciences, 109(103297), 103297, https://doi.org/10.1016/j.jsames.2021.103297.

Gutiérrez-Aguilar, F., Schaaf, P., Solís-Pichardo, G., Arrieta-García, G. F., Hernández-Treviño, T., Linares-López, C., 2021b, Phase equilibrium modelling of the amphibolite facies metamorphism in the Yelapa-Chimo Metamorphic Complex, Mexico: Geoscience Frontiers, 12(1), 293-312, https://doi.org/10.1016/j.gsf.2020.05.001.

Hawthorne, F.C., Oberli, R., Harlow, G.E., Maresch, WV., Martin, R.F., Schumacher, J.C., Welch, M.D., 2012, Nomenclature of the amphibole supergroup: The American Mineralogist, 97(11-12), 2031-2048, https://doi.org/10.2138/am.2012.4276.

Henry, D.J., 2005, The Ti-saturation surface for low-to-medium pressure metapelitic biotites: Implications for geothermometry and Ti-substitution mechanisms: The American Mineralogist, 90(2-3), 316-328, https://doi.org/10.2138/am.2005.1498.

Holland, T., Blundy, J., 1994, Non-ideal interactions in calcic amphiboles and their bearing on amphibole-plagioclase thermometry: Contributions to Mineralogy and Petrology, 116(4), 433-447, https://doi.org/10.1007/bf00310910.

Holness, M.B., Stock, M.J., Geist, D., 2019, Magma chambers versus mush zones: constraining the architecture of sub-volcanic plumbing systems from microstructural analysis of crystalline enclaves: Philosophical Transactions of the Royal Society A, 377(2139), 20180006.

Johnson, K.T., Dick, H.J., Shimizu, N., 1990, Melting in the oceanic upper mantle: an ion microprobe study of diopsides in abyssal peridotites: Journal of Geophysical Research:Solid Earth, 95(B3), 2661-2678.

Kirkland, C.L., Smithies, R.H., Taylor, R.J.M., Evans, N., McDonald, B., 2015, Zircon Th/U ratios in magmatic environs: Lithos, 212, 397-414.

Kelley, S., 2002, Excess argon in K-Ar and Ar-Ar geochronology: Chemical Geology, 188, 1-22.

Konrad, K., Koppers, A.A.P., Balbas, A.M., Miggins, D.P., Heaton, D.E., 2019, Dating clinopyroxene phenocrysts in submarine basalts using $^{40}Ar/^{39}Ar$ geochronology: Geochemistry, Geophysics, Geosystems, 20, https://doi.org/10.1029/2018GC007697.

Koszowska, E., Wolska, A., Zuchiewicz, W., Cuong, N.Q., Pécskay, Z., 2007, Crustal contamination of Late Neogene basalts in the Dien Bien Phu Basin, NW Vietnam: Some insights from petrological and geochronological studies: Journal of Asian Earth Sciences, 29(1), 1-17. https://doi.org/10.1016/j.jseaes.2005.12.003.

Locock, A.J., 2014, An Excel spreadsheet to classify chemical analyses of amphiboles following the IMA 2012 recommendations:Computers and Geosciences, 62, 1-11, https://doi.org/10.1016/j.cageo.2013.09.011.

Luo, B.-J., Zhang, H.-F., Xu, W.-C., Guo, L., Pan, F.-B., Yang, H., 2015, The middle Triassic Meiwu batholith, west Qinling, central China: Implications for the evolution of compositional diversity in a composite batholith: Journal of Petrology, 56(6), 1139-1172, https://doi.org/10.1093/petrology/egv032.

Montaño-Cortes, P.C., Molina-Garza, R.S., Iriondo, A., 2019, Paleomagnetismo e isotopos de Hf en rocas del Cretácico Inferior del Terreno Guerrero, Bahía Chamela e Isla Cocinas (Jalisco, Mexico): implicaciones tectónicas: Revista Mexicana de Ciencias Geológicas, 36(3), 289-307, https://doi.org/10.22201/cgeo.20072902e.2019.3.1048.

Moyen, J.F., Janoušek, V., Laurent, O., Bachmann, O., Jacob, J.B., Farina, F., Fiannacca, P., Villaros, A. 2021, Crustal melting vs. fractionation of basaltic magmas: Part 1, granites and paradigms: Lithos, 402, 106291, https://doi.org/10.1016/j.lithos.2021.106291.

Morán-Zenteno, D.J., Martiny, B.M., Solari, L., Mori, L., Luna-González, L., González-Torres, E.A., 2018, Cenozoic magmatism of the Sierra Madre del Sur and tectonic truncation of the Pacific margin of southern Mexico: Earth-Science Reviews, 183, 85-114, https://doi.org/10.1016/j.earscirev.2017.01.010.

Mutch, E.J.F., Blundy, J.D., Tattitch, B.C., Cooper, F.J., Brooker, R.A., 2016, An experimental study of amphibole stability in low-pressure granitic magmas and a revised Al-in-hornblende geobarometer: Contributions to Mineralogy and Petrology, 171(10), https://doi.org/10.1007/s00410-016-1298-9.

O'Driscoll, B., Emeleus, C.H., Donaldson, C.H., Daly, J.S., 2010, Cr-spinel seam petrogenesis in the rum layered suite, NW Scotland: Cumulate assimilation and in situ crystallization in a deforming crystal mush: Journal of Petrology, 51(6), 1171-1201, https://doi.org/10.1093/petrology/egq013.

Ortega-Gutiérrez, F., Elías-Herrera, M., Morán-Zenteno, D.J., Solari, L., Luna-González, L., Schaaf, P., 2014, A review of batholiths and other plutonic intrusions of Mexico: Gondwana Research, 26(3-4), 834-868, https://doi.org/10.1016/j.gr.2014.05.002.

Panseri, M., 2007, Il Batolite di Manzanillo (Messico sud-occidentale): Analisi Strutturale, Petrologia, Geochimica e Geocronologia: Milan, Italy, Università degli studi di Milano, Dottorato di Ricerca XX Ciclo Scienze della Tierra, Ph.D. Thesis, 122 pp.

Pearce, J.A., 1983, Role of the sub-continental lithosphere in magma genesis at active continental margins, *in* Hawkesworth, C.J., Norry, M.J. (eds.), Continental basalts and mantle xenoliths: Shiva Publications, p. 272.

Prouteau, G., Scaillet, B., Pichavant, M., Maury, R, 2001, Evidence for mantle metasomatism by hydrous silicic melts derived from subducted oceanic crust: Nature, 410(6825), 197-200, https://doi.org/10.1038/35065583

Putirka, K.D., 2008, Thermometers and barometers for volcanic systems: Reviews in Mineralogy and Geochemistry, 69(1), 61-120, https://doi.org/10.2138/rmg.2008.69.3.

Renna, M.R., Tribuzio, R., 2011, Olivine-rich troctolites from Ligurian ophiolites (Italy): Evidence for impregnation of replacive mantle conduits by MORB-type melts: Journal of Petrology, 52(9), 1763-1790. https://doi.org/10.1093/petrology/egr029.

Ridolfi, F., Renzulli, A., Puerini, M.., 2010, Stability and chemical equilibrium of amphibole in calc-alkaline magmas: an overview, new thermobarometric formulations and application to subduction-related volcanoes: Contributions to Mineralogy and Petrology, 160(1), 45-66. https://doi.org/10.1007/s00410-009-0465-7.

Salazar-Juárez, J., 2017, Evolución magmática del complejo intrusivo de Jilotlán (Jalisco): Mexico City, Universidad Nacional Autónoma de México, M.Sc.thesis, 138 pp.

Schaaf, P., 1990, Isotopengeochemische Untersuchungen an granitoiden Gesteinen eines aktiven Kontinentalrandes. Alter und Herkunft der Tiefengesteinskomplexe an der Pazifikküste Mexikos zwischen Puerto Vallarta und Acapulco: Germany, Universität München, Ph.D. Thesis, 203 pp.

Schaaf, P., Díaz-López, F., Gutiérrez-Aguilar, F., Solís-Pichardo, G., Hernández-Treviño, T., Arrieta-García, G., Solari, L., Ortega-Obregón, C., 2020, Geochronology and geochemistry of the Puerto Vallarta igneous and metamorphic complex and its relation to Cordilleran arc magmatism in northwestern Mexico: Lithos, 352-353(105248), 105248, https://doi.org/10.1016/j.lithos.2019.105248.

Schaaf, P., Corona-Chávez, P., Ortiz Joya, G., Solís-Pichardo, G., Arrieta García, G., Hernández Treviño, T., Poli, S., 2022, Magma hybridization, mingling, and recycling in the Manzanillo plutonic complex, Mexican Cordillera: International Geology Review, 64(9), 1248-1269, https://doi.org/10.1080/00206814.2021.1919931.

Schaltegger, U., Davies, J.H., 2017, Petrochronology of zircon and baddeleyite in igneous rocks: Reconstructing magmatic processes at high temporal resolution: Reviews in Mineralogy and Geochemistry, 83(1), 297-328.

Schoene, B., Schaltegger, U., Brack, P., Latkoczy, C., Stracke, A., Günther, D., 2012, Rates of magma differentiation and emplacement in a ballooning pluton recorded by U–Pb TIMS-TEA, Adamello batholith, Italy: Earth and Planetary Science Letters, 355-356, 162-173, https://doi.org/10.1016/j.epsl.2012.08.019.

Sisson, T.W., Grove, T.L., 1993, Experimental investigations of the role of H_2O in calc-alkaline differentiation and subduction zone magmatism: Contributions to Mineralogy and Petrology, 113(2), 143-16, https://doi.org/10.1007/bf00283225

Solé, J., Salinas, J.C., González-Torres, E., Cendejas Cruz, J.E., 2007, K/Ar ages of 54 igneous and metamorphic rocks from western, central and southern Mexico: Revista Mexicana de Ciencias Geologicas, 24(1), https://www.scielo.org.mx/scielo.php?pid=S1026-87742007000100009&script=sci_abstract&tlng=pt.

Straub, S.M., Zellmer, G.F., Gómez-Tuena, A., Espinasa-Pereña, R., Martin-del Pozzo, A.L., Stuart, F.M., Langmuir, C.H, 2014, A genetic link between silicic slab components and calc-alkaline arc volcanism in central Mexico: Geological Society Special Publication, 385(1), 31-64, https://doi.org/10.1144/sp385.14.

Triantafyllou, A., Berger, J., Baele, J.-M., Mattielli, N., Ducea, M. N., Sterckx, S., Samson, S., Hodel, F., Ennih, N., 2020, Episodic magmatism during the growth of a Neoproterozoic oceanic arc (Anti-Atlas, Morocco): Precambrian Research, 339(105610), 105610, https://doi.org/10.1016/j.precamres.2020.105610.

Valencia, V.A., Righter, K., Rosas-Elguera, J., López-Martínez, M., Grove, M., 2013, The age and composition of the pre-Cenozoic basement of the Jalisco Block: implications for and relation to the Guerrero composite terrane: Contributions to Mineralogy and Petrology., 166(3), 801-824, https://doi.org/10.1007/s00410-013-0908-z.

Vermeesch, P., 2018, IsoplotR: A free and open toolbox for geochronology: Geoscience Frontiers, 9(5), 1479-1493, https://doi.org/10.1016/j.gsf.2018.04.001.

Villanueva-Lascurain, D., Solís-Pichardo, G., Schaaf, P., Hernández-Treviño, T., Salazar-Juárez, J., Corona-Chávez, P., 2016, Age and origin of the gabbros in the Jilotlán pluton, Jalisco: primitive magmatic rocks in the southern part of the Guerrero terrane: Revista Mexicana de Ciencias Geológicas, 33(1), 136-156, https://www.scielo.org.mx/scielo.php?pid=S1026-87742016000100136&script=sci_arttext&tlng=en.

Vite Sánchez, O., 2019, Interacción de rocas intrusivas y metamórficas en el batolito de Puerto Vallarta (Zona de Punta Mita): evidencias geoquímicas y geocronológicas: Mexico City, Mexico, Universidad Nacional Autónoma de México, M. Sc Thesis, 131 pp.

Whitney, D.L., Evans, B.W., 2010, Abbreviations for names of rock-forming minerals: American Mineralogist, 95(1), 185-187.

Woodhead, J.D., Eggins, S.M., Johnson, R.W., 1998, Magma genesis in the New Britain island arc: further insights into melting and mass transfer processes: Journal of Petrology, 39(9), 1641-1668.

Xie, F., Lang, X., Tang, J., Ma, D., Zou, B., 2019, Late Cretaceous magmatic activity in the southern Lhasa terrane: insights from the Dazhuqu hornblende gabbro and the Xietongmen granite porphyry: International Geology Review, 61(13), 1642-1665, https://doi.org/10.1080/00206814.2018.1531273.

Manuscript received: July 13, 2023
Corrected manuscript received: September 28, 2023
Manuscript accepted: September 29, 2023